Polymat

Contributions

Proceedings

Polymat Contributions

Polypeptides: from proteins to new approaches in polymer synthesis

Colin Bonduelle[1]

[1]*University of Bordeaux, CNRS, Bordeaux INP. LCPO(Laboratoire de Chimie des Polymères Organiques), ENSCBP, 16 avenue Pey Berland, F-33600, Pessac, France. colin.bonduelle@enscbp.fr*

In nature, proteins provide physiological support for cells, tissues and organs, but they also participate in a myriad of metabolic processes, notably via the catalysis of biochemical reactions, the regulation of cellular signals and the transport of molecules. Against this backdrop, the use of proteins in the design of new drugs or in the manufacture of new materials is extremely promising for many applications.[1] In particular, and to promote sustainability, they are polymers of choice, both degradable and metabolizable.

Producing proteins still remains a challenge: methodologies using genetic engineering or synthetic biology are often very costly and require extensive development of specific biotechnology platforms, which further limits the scale and scope of these preparation routes.[2] The design of "synthetic proteins" via chemistry (*de novo* synthesis) is an alternative approach which aims to reproduce, without biology, the macromolecular peptide structure of these proteins. In this context, there are two major preparation routes:

- **Complete reproduction of the primary sequence, based on multi-step synthesis methodologies** known as iterative coupling (e.g. Merryfield's supported synthesis, which won the Nobel Prize in 1963, SPPS *Figure 1*).[3] These methods enable the preparation of controlled sequence oligomers,[4] but the use of a lengthy process combining several steps also means that i) the size of the macromolecules is often limited, ii) cost-effective production on a gram scale is often a challenge and iii) the preparation of new synthetic structures requires a specific synthesis scheme which needs to be optimized.[5] These three limitations are significant drawbacks that often hinder the use of peptide synthesis on a large scale, for example to design biomaterials.

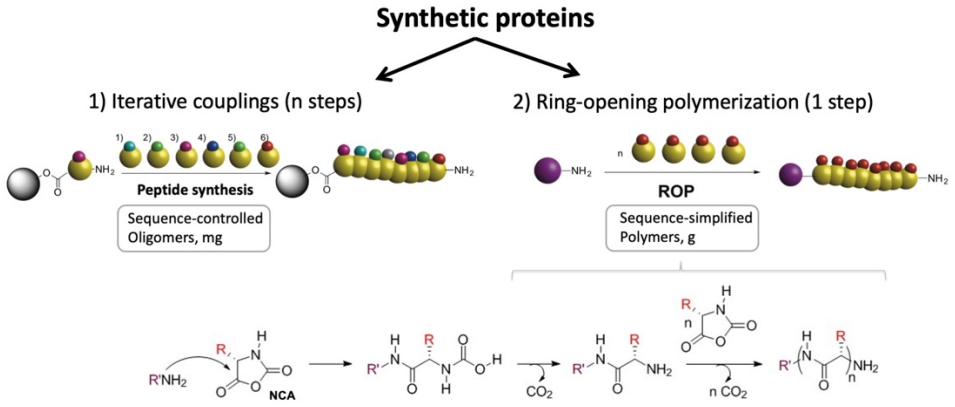

Figure 1. Synthetic proteins can be prepared by peptide synthesis (iterative coupling) or by ring-opening polymerization (ROP) of N-carboxyanhydride (NCA). In the diagram, the yellow balls represent amino acids, the smaller balls in a different color, their side chains.

- **A more efficient process for preparing macromolecular peptide structures is the one-step ring-opening polymerization** (ROP *Figure 1*) of amino acid-derived N-carboxyanhydride (NCA) monomers.[6] The peptide polymers or polypeptides resulting from this polymerization are simpler macromolecules than natural proteins: they are homopolymers or copolymers with statistical primary sequences, and so on. Compared with other polymers, polypeptides combine the advantageous characteristics of synthetic macromolecules (solubility, processing, elasticity, etc.) with those of natural proteins (secondary structure, functionality, biocompatibility, etc.).[7] A major research challenge for this family of polymers is to better reproduce the structural and functional properties of their natural models: proteins (for example, to confer specific therapeutic or catalytic activities).

1. Copolymerization to mimic the activity and topology of antimicrobial peptides

For many living systems, the response to infection involves the secretion of antimicrobial peptides. These sequence-controlled macromolecules have a wide variety of chemical structures, and possess key structural features that give them their biological properties: the nature of the amino acids that make up the peptide backbone, the overall hydrophobicity, the overall charge of the macromolecule, its topology, its structuring and so on.[8] In particular, antimicrobial peptides are often cyclic (c-AMPs): compared with their linear analogues, they have lower toxicity and target certain bacteria more selectively.

In this context, we have developed a one-step copolymerization method to mimic the sequence and topology of these c-AMPs. We first developed the synthesis of various glycine-derived monomers that are N-substituted with hydrophobic (*Figure 2, red*) and cationic (*Figure 2, blue*) moieties. In a second step, we implemented their polymerization by ROP: our work enabled us to reveal a new route to cyclic macromolecules thanks to the use of a particular catalyst, LiHMDS. During polymerization, the latter favors a mechanism in which the initiator and polymer ends are stabilized by the same complex thanks to the Li atom (*figure 2*). This methodology enabled us to modulate polymer size and composition by adjusting the stoichiometry of NCA monomers and LiHMDS.[9]

As part of a collaboration with the Pasteur Institute, we finally assessed the antibacterial potential of our copolymers on *C. difficile*, a pathogen that causes very serious nosocomial diseases, especially in the elderly. An in-depth study of the structure/activity relationships was carried out by modulating certain macromolecular parameters: hydrophobic content, nature of the monomer (hydrophobic and cationic side chains), degree of polymerization, etc. This study enabled us to define specific antibacterial properties of our copolymers. This study enabled us to define macromolecular pharmacophores for selectively killing this bacterium.[9] A patent has been filed and we are currently developing this approach with an industrial partner with a view to commercializing the results of our work.[10]

The interesting thing about this copolymerization approach is that simple copolymerization enables us to mimic the biological activity normally associated with the

complex topology and primary sequence of natural proteins/peptides, in this case c-AMPs. This simplification of design opens up many new prospects, such as making it much easier to produce peptide structures of interest for infectiology (oral treatment, etc.).

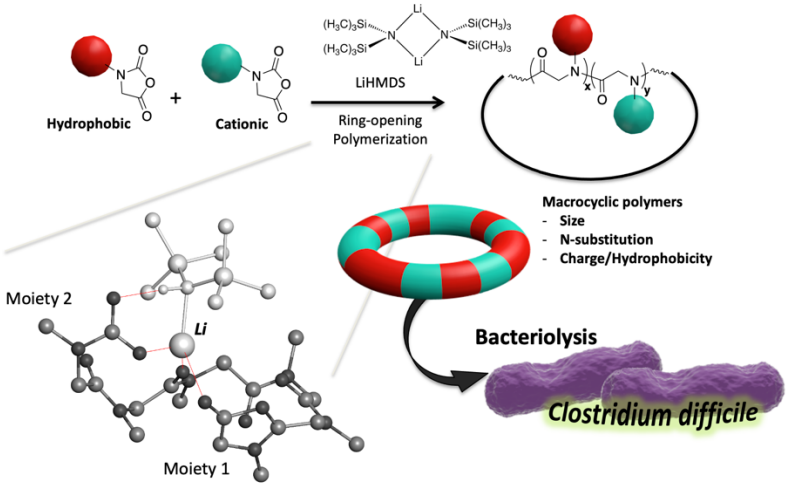

Figure 2. Peptide copolymers can be simplified analogues of antimicrobial peptides. They are easy to synthesize, allowing multiple functions to be combined with macromolecular engineering to mimic the cyclic topology of natural models.

2. Peptide polymers to mimic protein conformation and adaptation

Peptide polymers are simpler than proteins: one or more amino acids are repeated several times in an uncontrolled primary sequence. Despite this, peptide polymers retain the property of forming secondary structures, rigid blocks stabilized locally by hydrogen bonds resulting in a preferred conformation.[7] Historically, peptide polymers have thus served as models for elucidating protein structure: the α-helix and β-sheet secondary structures discovered by Pauling and Corey at the California Institute of Technology in 1951, two years before Watson and Crick solved the structure of DNA (*Figure 3*).[11]

Thanks to their structuring, peptide polymers are ideal candidates for mimicking adaptive protein systems that undergo conformational changes in response to various external stimuli (temperature, pH, etc.). We have demonstrated that biologically relevant stimuli such as pH, redox changes or metal complexation can trigger a reversible conformational transition of these polymers, as can be observed in nature with metalloproteins.[12] We have also developed a new class of smart polypeptides, called nucleopolypeptides, which are analogues of nucleoproteins, proteins that interact specifically with nucleic acids in the cell nucleus of living systems.[13] Our polymers have side chains functionalized with nucleobases to promote specific pairing with DNA side chains (*Figure 4*). In the presence of certain DNA sequences, the conformational adaptation of our polymers optimizes their interaction with nucleobases, a property uncommon outside protein systems.

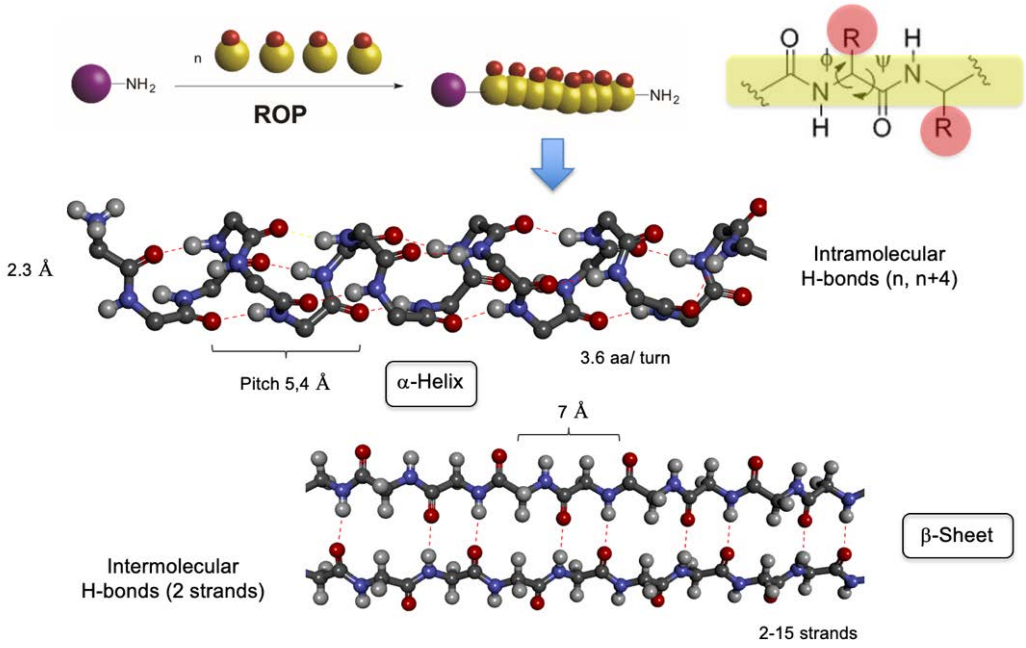

Figure 3. Polypeptides are simplified analogues of proteins that reproduce their natural structures. Two representative examples are shown here: the alpha helix, a conformation stabilized by intramolecular hydrogen bonds, and the beta leaflet, a conformation stabilized by intermolecular hydrogen bonds.

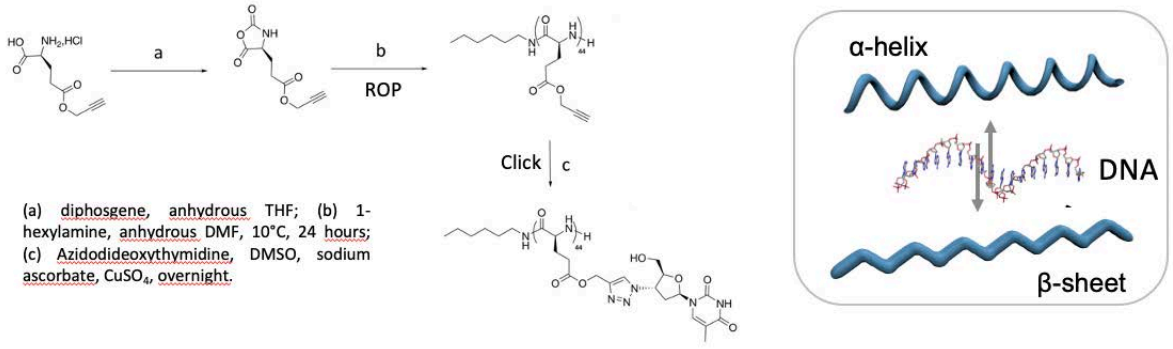

Figure 4. Nucleopolypeptides are simplified analogues of nucleoproteins (e.g. leucine zipper). They are polymers prepared in two simple steps: polymerization (ROP) and Huisgen cycloaddition (Click). In the presence of certain DNA sequences, these polymers can adapt their structures to better interact with adenosines, an interaction that has been studied in solution and on the surface of nanomaterials.

3. NCA polymerization in water: simplified protein translation

Efficiently forming peptide bonds in aqueous media is still a challenge for synthetic chemistry (*Figure 5*), whereas protein translation is a highly efficient aqueous biological process.[14] The particular reactivity of amino acid-derived NCAs in this same aqueous phase,

if their hydrolysis can be controlled, means that protein translation can be simplified by a simple polymerization reaction in water. Following this principle, we have, for example, developed the ROP of NCAs by adapting the so-called PISA (polymerization induced by self-assembly) processes to obtain amphiphilic polypeptides.[15] This process, known as ROPISA, enables the formation of block copolymers in aqueous phase, with one hydrophilic and one hydrophobic part, forming nanostructures which have the particularity of being non-spherical (anisotropic). This means that their properties, e.g. optical, change according to their collective orientation, which is rarely observed with polymer nanoparticles. A patent has been filed, and we have established that the secondary structuring of peptide polymers is responsible for the efficiency of the process, as well as for the specific shape of the nano-objects.[16]

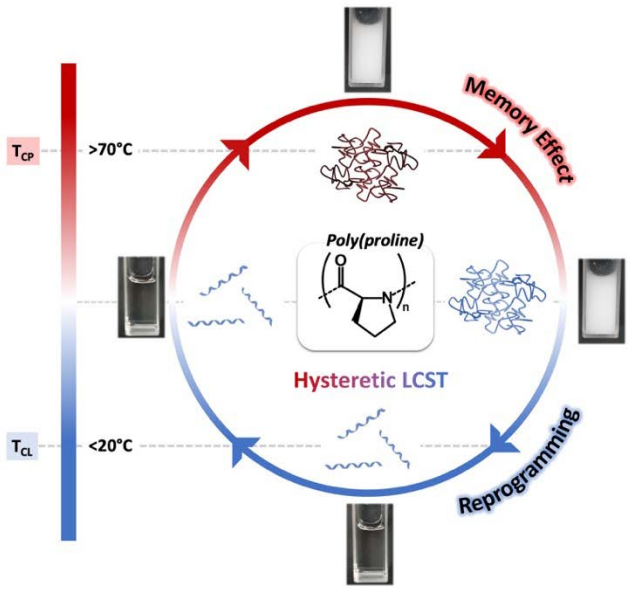

Figure 5. Synthetic polymers made from L-proline monomer units exhibit temperature-induced aggregation in water with unprecedented hysteresis. This protein-like behavior is robust and governed by the chirality of the proline units. It opens the way to new processes/materials that will be driven by simple changes in temperature or ionic strength.

Very recently, by studying the polymerization in water of a specific monomer, NCA proline, in this case without self-assembly, we also discovered that the conformation of polypeptides gave rise to an original thermal sensitivity thanks to the aqueous phase. The macromolecules we synthesized retain the memory of their aggregation, a property so far observed in biology with more complex protein systems (proteins derived from elastin, for example), but which was difficult to reproduce with synthetic polymers obtained, for example, by radical chemistry (PNIPAM). The use of this hysteresis phenomenon could make it possible to design new processes/materials that can take advantage of this memory effect.[17]

In conclusion, these few representative examples show how amino acid-based synthetic polymers represent a unique class of biomimetic macromolecules because (1) they feature the same macromolecular skeleton as proteins, (2) they can be obtained on a large scale and in a single step using ring-opening polymerization methodology, (3) the random combination of amino acids makes it possible to reproduce certain properties of proteins that are attributed to their controlled sequences, (4) polymerization is a simple means of accessing complex topologies (non-linear : cyclic, branched, etc.), and (5) they can fold into different secondary structures as proteins do, giving them original physico-chemical properties.

References

[1] a) H. Zhang et al. *Adv. Mater.* **2020**, 32(6), 1906360; b) A.J.D. Silvestre et al. *J. Mater. Chem. B*, **2014**, 2, 3715.
[2] J.K. Montclare et al. *Adv. Health. Mater.* **2019**, 8(11), 1801374.
[3] R. B. Merrifield *J. Am. Chem. Soc.* **1963**, 85, 2149.
[4] J. F. Lutz et al. *J. Am. Chem. Soc.* **2015**, 137, 16, 5629.
[5] C. H. Wong and S. C. Zimmerman, *Chem. Commun.* **2013**, 49, 1679.
[6] G. Qiao et al. *Chem. Soc. Rev.* **2020**,49, 4737.
[7] C. Bonduelle *Polym. Chem.* **2018**, 9, 1517.
[8] C. Bonduelle et al. *Biomacromolecules* **2021**, 22(1), 57.
[9] C. Bonduelle et al. *J. Am. Chem. Soc.* **2021**, 143, 3697.
[10] Antimicrobial cationic peptoid and N-substituted peptidic copolymers, preparation and uses thereof. WO2022175319A1.
[11] D. Eisenberg *Proc. Natl. Acad. Sci. U. S. A.* **2003**, 100, 11207.
[12] C. Bonduelle et al. *Polym. Chem.* **2018**, 9(30), 4077.
[13] C. Bonduelle et al. a) *Chem. Commun.* **2017**, 53, 7501; b) *Biomacromolecules* **2018**, 19, 4068; c) *Polymers*, **2020**, 12, 1357.
[14] J. W. Bode et al. *Nature* **2011**, 480, 471.
[15] C. Bonduelle et al. *Angew. Chem. Int. Ed.* **2020**, 59, 622.
[16] Method for preparing controlled peptide-based polymers and copolymers in an aqueous solution WO2021043865A1; C. Bonduelle et al. *Polym. Chem.* **2021**, 12, 6242.
[17] C. Bonduelle et al. *Angew. Chem. Int. Ed.* **2022**, 61, 46, e202209530.

Acknowledgements (10 pt)

The author acknowledges the professors Marcela Ayala (IBT, UNAM) and Abel Moreno (IQ, UNAM) for helpful discussions. This work was supported by the ECOS Nord exchange program (grant M19P05) and CONACYT ANUES.

Manufacture of Cu20Sn syntactic foams with Fe hollow spheres

L. E. Carranza[1], L. Béjar[1], C. Aguilar[2], I.A. Figueroa[3], I. Alfonso[4]

[1] Facultad de Ingeniería Mecánica. Universidad Michoacana de San Nicolás de Hidalgo. Edificio W, Ciudad Universitaria. CP 58000, Morelia, Michoacán, México. lecarranza@iim.unam.mx
[2] Departamento de Ingeniería Metalúrgica y Materiales. Universidad Técnica Federico Santa María, Av. España 1680, Casilla 110-V, Valparaíso, Chile.
[3] Instituto de Investigaciones en Materiales, Universidad Nacional Autónoma de México, Circuito Exterior S/N, Cd. Universitaria, C.P. 04510, Ciudad de México, México.
[4] Instituto de Investigaciones en Materiales, Unidad Morelia, Universidad Nacional Autónoma de México, Campus Morelia UNAM. Antigua Carretera a Pátzcuaro No. 8701, Col. Ex-Hacienda de San José de la Huerta. C.P. 58190, Morelia, Michoacán. México.

Introduction

Metal foams are materials that have undergone significant development in recent years due to their advantages in engineering applications, because these type of materials have a combination of unique characteristics, such as their light structure and their good physical, chemical and mechanical properties. To refer to this materials, the term metal foam is defined as any metallic material with deliberately introduced pores.[1] Metal foams can be classified as i) open cell foams: these are the ones that have interconnected porosity; ii) closed-cell foams: where the pores are not interconnected, and iii) metal foams reinforced with hollow particles, also known as syntactic foams [2]. In recent years, there has been increasing interest in the study of syntactic foams due to their adaptable properties and applications in various types of industries. Syntactic metallic foams are composite materials that are made up of hollow particles embedded in a metallic matrix.
Metal matrix syntactic foams are a highly competitive material in the industry: aerospace, biomedical, electronics and structural applications [3]. This work includes a method for manufacturing syntactic foams of a $Cu_{20}Sn$ alloy using hollow iron spheres as a porosity generator and infiltration method as a manufacturing process.

Experimental

The manufacturing process begins with the acquisition of materials, for which the $Cu_{20}Sn$ alloy is manufactured using an induction furnace with a controlled argon atmosphere. This alloy has a density of 8.79g/cm^3. The material used as a porosity generator are iron hollow spheres, which are acquired by the company Hollomet GmbH, these spheres have a density of 0.7 g/cm^3 and a wall thickness of 130 um, the spheres were sieved to use them in a uniform size with a diameter of 3 mm, the materials are shown in Figure 1.

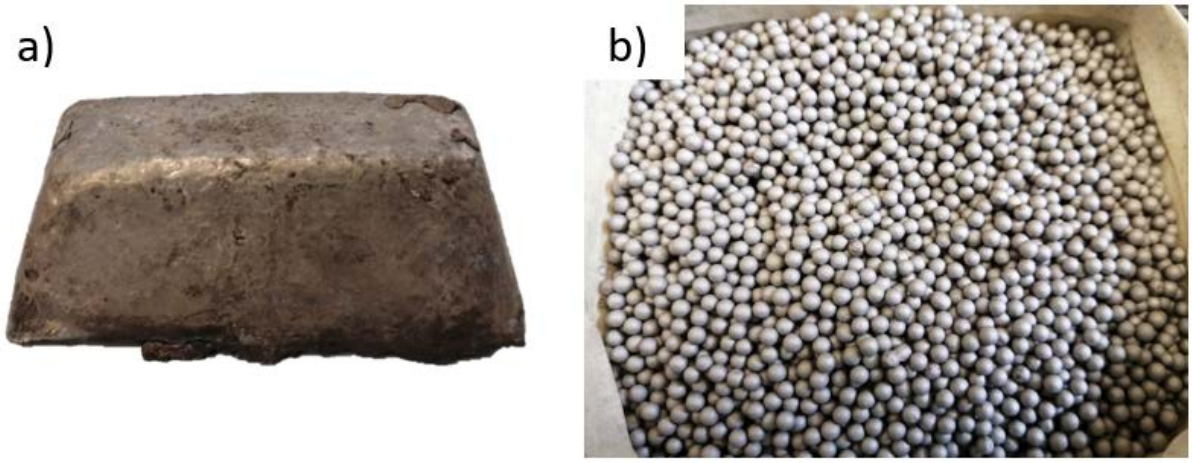

Figure 1. Materials used for the manufacture of syntactic foams: a) Cu20Sn alloy, b) Hollow iron spheres.

As part of the manufacturing of the spheres, the process begins by pouring the spheres into the infiltration chamber shown in Figure 2a, where they are placed randomly. Afterwards, the hollow spheres are sintered at 1000°C for one hour. This is with the objective of forming a preform and ensuring that at the time of infiltration there is a uniform distribution of these in the foam. Figure 2b shows the result of sintering the spheres.

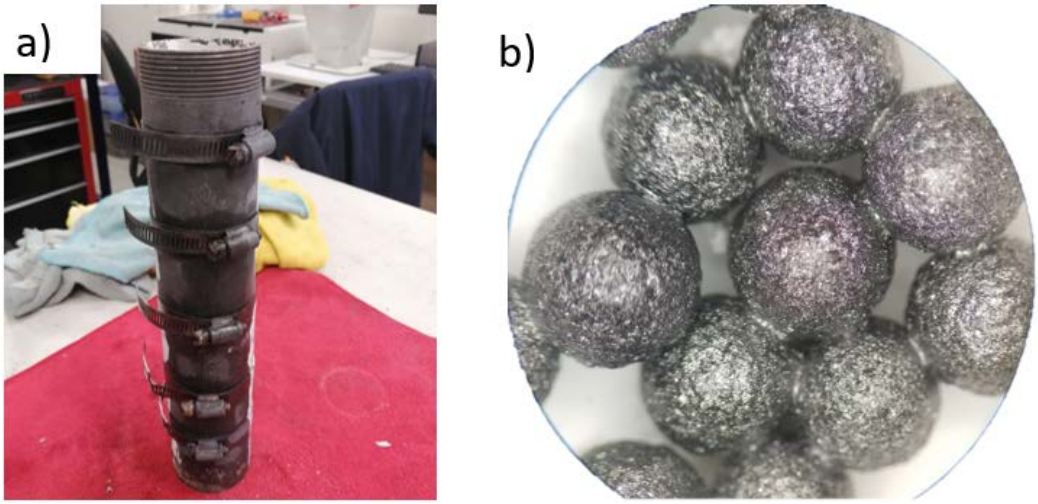

Figure 2. a) Infiltration chamber to manufacture metal foams, b) iron spheres sintered at 1000°C for 1 hour.

To carry out the infiltration of the metal through the iron spheres, the metal is loaded into the infiltration chamber and an injection nozzle is placed. The infiltration is carried out at 950°C for 30 min using Ar pressure to ensure that the metal flows between the previously sintered

spheres. The sintering and infiltration process are carried out in a resistance furnace. The equipment assembly is shown in Figure 3.

Figure 3. Assembly of the infiltration device and injection nozzle for the manufacture of metal foams.

As a final step, the mold is allowed to cool and the foam is removed from the mold.

Results and discussion

As part of the results, the syntactic foams were obtained, these were machined to obtain the following measurements: 3 cm in diameter and 2.5 cm in height, these measurements satisfied the conditions for the density measurement, this was carried out using the Archimedean method. Likewise, the measurement of the porosity of the foams obtained by image analysis was carried out using the program ImageJ, obtaining approximately a porosity of 60%. Figure 4 shows the obtained syntacic metal foam using the method described above.

Figure 4. Syntactic $Cu_{20}Sn$ metal foam using iron hollow spheres.

Conclusions

The manufacturing route for syntactic metal foams mentioned in this article turned out to be a good process, because samples of $Cu_{20}Sn$ alloy syntactic foams were satisfactorily obtained using hollow iron spheres.

References

[1] H.P. Degischer and B. Kriszt, Handb. Cell. Met., Production, Processing, Applications. **2002**.

[2] Gupta N, Metal Matrix Syntactic Foam: Processing, microstructure, properties, applications. Chapter 1, ed. Gupta N, Rohatgi P, DEStech Publ. In, **2015**.

[3] R. Thiyagarajan and M. Senthil kumar, “A Review on Closed Cell Metal Matrix Syntactic Foams: A Green Initiative towards Eco-Sustainability,” *Mater. Manuf. Process.*, **2021,** vol. 36, no. 12, pp. 1333–1351, doi: 10.1080/10426914.2021.1928696.

Acknowledgements

Authors would like to acknowledge the financial support from project UNAM PAPIIT IN102322.

Synthesis of amphiphilic block copolymers MPEG/PEG-b-PNIPAM and MPEG/PEG-PCL-PNIPAM for drug delivery systems

Gladys de los Santos[1], Luis E. Elizalde[1], Luis A. García[1], Liliana T. Corona[1], J. Carlos Romero[1], Angélica Velázquez[1]

[1]Centro de Investigación en Química Aplicada. Blvd Enrique Reyna 140, Saltillo, Coah. MÉXICO
gladys.delossantos@ciqa.edu.mx

Nanotechnology appeared almost 50 years ago, with the possibility of handling atoms and molecules in nanometric size. Over the past years, polymeric nanobiomaterials have bloomed because of the rapid development of synthetic methods, control of molecular architecture, characterization, and interdisciplinary research between polymer science and biology. Particularly, nanocarriers have contributed to the development of precision medicine, increasing the efficacy of bioactive molecules by prolonging availability in the intended final site of action.

Secondary side effects, associated with toxicity and low water solubility, increase the demand for new specific drug delivery systems (DDS) to treat some complex diseases. DDS emerged as a promising alternative to medical carriers for the loading and releasing drugs or bioactive molecules for specific diseases in specific action sites[1]. The main challenges for these systems are the specific delivery to cells and tissues at the right time and in a safe and reproducible manner, affinity to the receptor, simultaneous delivery of 2 or more drugs, and drug traceability. DDS are engineered devices used to transport a pharmaceutical compound through the body, to be then released in a controlled manner and in a specific site. They should be stable, exhibit no early cargo/release, non-toxic, biodegradable, and water soluble.

[1] B. Twaites, C. de las Heras Alarcon, C. Alexander, *Synthetic polymers as drugs and therapeutics, J. Mater. Chem*. 15 (2005) 441–455

Amphiphilic block copolymers mainly synthesized from PEGylated water-soluble and biocompatible macromolecules appeared to load small amounts of hydrophobic drugs, emphasizing the necessity to get defined architectures to trap organic molecules. Here, we report the synthesis of some hydrophilic biocompatible and biodegradable systems for DDS, which are thermosresponsive materials with a lower critical solution temperature (LSCT) near to human body temperature, enabling their use in a wide range of bio-applications[2,3]. The first system is a thermoresponsive amphiphilic block copolymer prepared from hydrophilic poly(ethylene oxide) (PEG) and poly(α-methylene oxide) (MPEG) and hydrophobic monomers N-isopropyl acrylamide (NIPAM) as the second monomer to get materials in nanometric size able to self-aggregate in order to be used for DDS. The final nanocarrier from system 1 (PEG/MPEG-b-PNIPAM) has been functionalized with a triazole group at the end of the polymer chain to trap metallic nanoparticles. The second system is an ABC block copolymer based on poly(ethylene or α-methylene oxide)-polycaprolactone[4] and poly (N-isopropyl acrylamide)[5] (PEG/MPEG-PCL-PNIPAM). Polymerization techniques such as ROP and the controlled radial method ARGET-ATRP were used for preparation. Characterization data were obtained from MALDI, IR, ^{1}H and ^{13}C-RMN, TGA, DSC, and Mn by GPC and ^{1}H-RMN, indicating the proper preparation of amphiphilic block copolymers. The chemical structures of both systems can be appreciated in Figure 1.

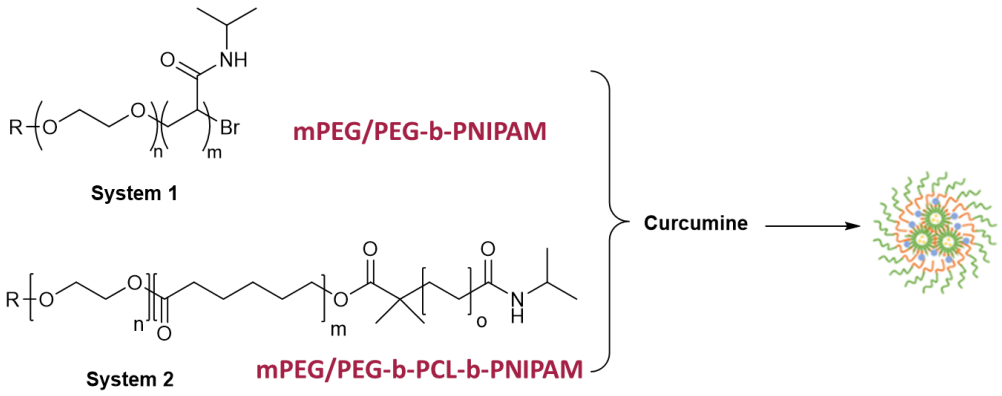

Figure 1. General scheme of amphiphilic block copolymers for DDS

[2] Ghezzi, M.; Pescina, M.; Padula, C.; Del Favero, E.; Cantú, L.; Nicoli, S.; *Polymeric micelles in drug delivery: an insight of the techniques for their characterization and assessment in biorelevant conditions; Journal of Controlled Released* (2021) 332, 312-336; https://doi.org.10.1016/j.conrel.2021.02.031

[3] A. Chan, R. P. Orme, R. A. Fricker, P. Roach; *Remote and local control of stimuli responsive materials for therapeutic applications, Advanced Drug Delivery Reviews*, 65, 4, (2013), 497-514

[4] T. K. Dash, V. B. Konkimalla*, Poly-ϵ-caprolactone based formulations for drug delivery and tissue engineering: A review. Journal of Controlled Release*, 158(1), (2012), 15-33

[5] R. Jankaew, N. Rodkate, S. Lamlertthon, B. Rutnakornpituk, U. Wichai, G. Ross, *"Smart" carboxymethylchitosan hydrogels crosslinked with poly(N-isopropylacrylamide) and poly(acrylic acid) for controlled drug release. Polymer Testing*. 42 (2015), 26-36

After characterization, the lower Critical Solution Temperature (LCST) of amphiphilic block copolymers from System 1 was calculated by Light Dispersion Scattering, showing a phase transition near to human body temperature. This data is shown on Figure 2.

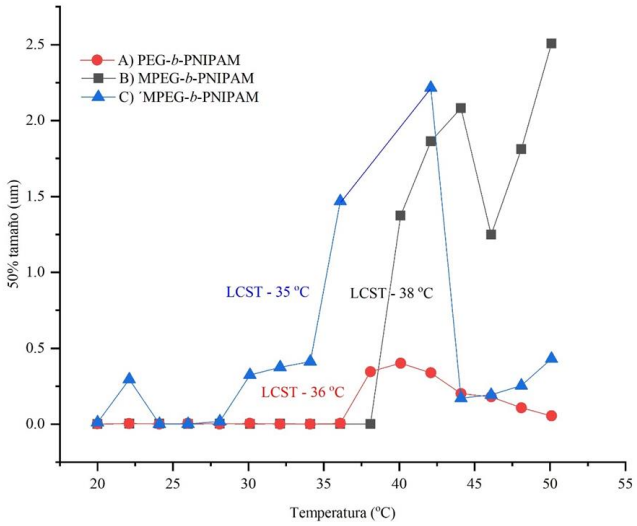

Figure 2. LCST of PEG/mPEG-b-PNIPAM amphiphilic block copolymers

Then, for System 2 LCST was also calculated at the same experimental conditions, results are presented on Figure 3.

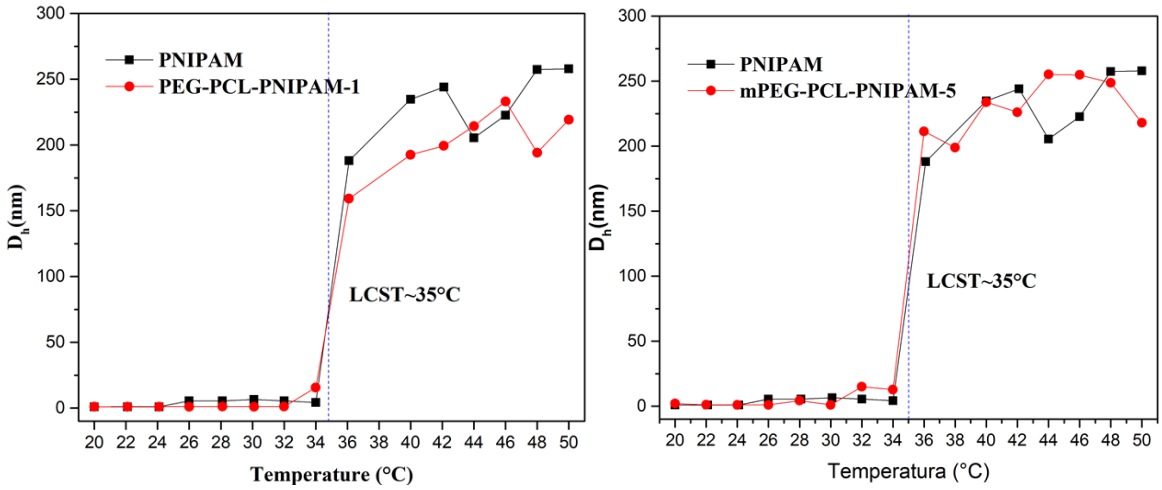

Figure 3. LCST for amphiphilic block copolymers PEG/mPEG-*b*-PCL-PNIPAM

For both systems, the loading and releasing of curcumin by copolymers was evaluated by UV-VIS. For this purpose, solutions of curcumin were prepared and incorporated into a copolymer THF/H_2O mixture solution after 24 h of stirring at room temperature, to be then heated at 40 °C for 30 minutes. Evaluation of loading and releasing parameters was done by UV-Vis. Results show that for some samples, about 50% of curcumin is loaded by the copolymer, and after heating at 40°C for 30 minutes, about 84% of the loaded curcumin is released. Best results were observed with the system mPEG-*b*-PNIPAM

CONCLUDING REMARKS

2 Types of amphiphilic block copolymers were synthesized and characterized, including the determination of LCST by DLS probing that they are thermoresponsive polymers at a temperature near to human body. These materials are able to load and release curcumin, but further investigation must be performed for the optimization of the system.

In an additional experiment, one of the systems was functionalized by click chemistry with an ethynyl pyridyl moiety to trap magnetic Hf ferrites which exhibit hyperthermia. These experiments would be used to demonstrate that these nano-carriers can be magnetically oriented to a specific action site[6].

Acknowledgements

We really appreciate the financial support received from CONAHCYT through Project **CB 2017-2018 A1-S-35972** to pursue this research.

[6] D. H. Kim, E. A. Vitol, J. Liu, S. Balasubramanian, D. J. Gostzola, E. E. Cohen, V. Novosad, E. Rozhkova, *Stimuli-responsive magnetic nanomicelles as multifunctional heat and cargo delivery vehicles; Langmuir*, 29, (2013), 7425-7432

Characterization and Mechanical Properties of Mg/HA biocomposites fabricated by liquid metal infiltration

Carmen H. Escalera[1], Ignacio A Figueroa[1*], M. Cristina Piña-Barba[1], Francisco Rodríguez-Gómez[2]

[1]Instituto de Investigaciones de Materiales, Universidad Nacional Autónoma de México, Ciudad Universitaria, Del. Coyoacán, CP 04510, CDMX, México.
[2]Facultad de Química, Universidad Nacional Autónoma de México, Ciudad Universitaria, Del. Coyoacán, CP 04510, CDMX, México.

**Corresponding author: iafigueroa@unam.mx*

Abstract

The present investigation is focused on the design of an interpenetrated Mg-Hydroxyapatite (Mg/HA) composite and its mechanical evaluation as a lightweight and high-strength material. In the study, HA porous preforms were obtained from cancellous bone. Then, infiltration with pure commercial Mg was applied using a liquid metal infiltration technique. Scanning electron microscopy, X-ray diffraction techniques, and image processing analysis analyzed the phases' microstructure, composition, and distribution. The Mg/HA biocomposite was subjected to compression tests to generate their stress-strain plots and to determine their mechanical properties. The results revealed that the HA preform was completely infiltrated by magnesium, producing a highly compact and lightweight biocomposite. The microstructural observation also showed that the Mg interacts with the HA; as a result, only MgO was identified as an additional phase. The Mg/HA composite enhanced the mechanical properties compared with the HA scaffold, attributing this behavior to the metallic material reinforcing the ceramic scaffold. The results obtained here could help design other biocomposite materials with different ranges of mechanical properties.

Introduction

In an effort to develop new materials to replace permanent fixtures that do not have to be removed by a second surgery, the design and preparation of magnesium (Mg)-based composites could be a solution. A biocomposite candidate can be designed with continuous networks to obtain a wide range of mechanical and biological properties and adjustable bioabsorption rates **[1]**. When a continuous network has different biodegradation rates, the bone tissue will grow toward the fastest biodegrading network. Meanwhile, the remaining networks maintained their geometrical shape and carried their physiological load for tissue ingrowth **[2]**. Hydroxyapatite (HA) is the most widely used reinforcement of the Mg compound due to its excellent biocompatibility, bioactivity, and osteoconduction properties with different dissolution rates **[3]**. In previous studies **[4-6]**, the suction casting technique successfully fabricated interpenetrating biomedical composites with an interconnected porous scaffold, usually prepared by replicating the porous structure with different

thermoplastics. However, the biodegradability of the thermoplastic was not considered; the fabrication of the composite will not prevent secondary medical surgeries. Based on the above, in this work, Mg was chosen as the matrix material and natural porous bone apatite (HA) was chosen as the reinforcement; both matrix and reinforcement could be absorbed at different rates, giving hard tissues time to heal. The design of this Mg/TCP composite by metal infiltration technique will help develop other composites in which at least one of the components can be from a natural source.

Materials and methods

The infiltration technique was carried out into a stainless-steel crucible previously coated with boron nitride, placing a magnesium ingot on the hydroxyapatite scaffold. The assembled crucible was placed into a resistance furnace preheated at a working temperature of 760° C. The melting was under an argon gas to protect the atmosphere and avoid Mg oxidation. After that, the infiltration of the magnesium through the interstices of the scaffold was attained by increasing the argon atmosphere pressure for 30 min. Finally, after 1 h, the crucible was removed from the furnace to cool down to room temperature by placing it on a copper block to induce a directional solidification. The schematic system of the infiltration process was described in our previous work **[7]**. The composite produced was machined into cylinders of 15 mm in length and 7 mm in diameter. The microstructural evolution of the investigated composites, Mg/HA, was studied through Scanning Electron Microscopy (SEM), operating at a nominal voltage of 20 kV in Back-Scattered Electron (BSE) mode. Complementary elemental mapping was carried out through Energy-Dispersive X-ray spectroscopy (EDS) coupled to the microscope. The analyzed samples were polished using the standard metallographic procedure, avoiding etching. The compression tests were carried out with a universal mechanical testing machine at a crosshead speed of 0.5 mm min^{-1} and a maximum load of 9,980 kg f (97.870 kN). Vickers hardness tests were performed using a microhardness tester applying a load of 0.98 N for 15 s indentation. Theoretical values, i.e., densities, yield strength, hardness, and ultimate compressive strength for obtained composites, were calculated using the rule of mixtures. For the calculations, the ceramic fraction, the metal matrix fraction, and the theoretical values of pure Mg and natural cancellous bone.

Results and discussion

The resulting Mg/HA composite was successfully obtained from infiltrated a natural cancellous bone with molten Mg, as shown in Figure 1. The resulting composite has a compact structure with a porosity of approximately 1%, i.e., the metal filled the interstices of the scaffold. The microstructural analyses and the EDS analyses show the final composite with a distribution of elements, including magnesium (Mg), calcium (Ca), phosphorous (P), and oxygen (O). Mg was observed as part of the matrix and in the interface between the metal and the ceramic (orange color). O(blue) was identified in the interface region with a length of 17 µm, attributed to forming a MgO phase as the metal and ceramic interaction. Finally, calcium (red) and phosphorous (green) were observed in the HA filament, which corresponds to the main elements content in the natural

bone. No other phases were identified. The formation of a MgO layer in the interface was attributed to a reaction between the scaffold and Mg; this reaction is quite different from the previously reported **[8]** because the cancellous bone has some remanent organic constituents that may interact with the molten Mg forming a thicker layer that the previously reported. More research is required to propose a chemical reaction mechanism for forming the MgO layer.

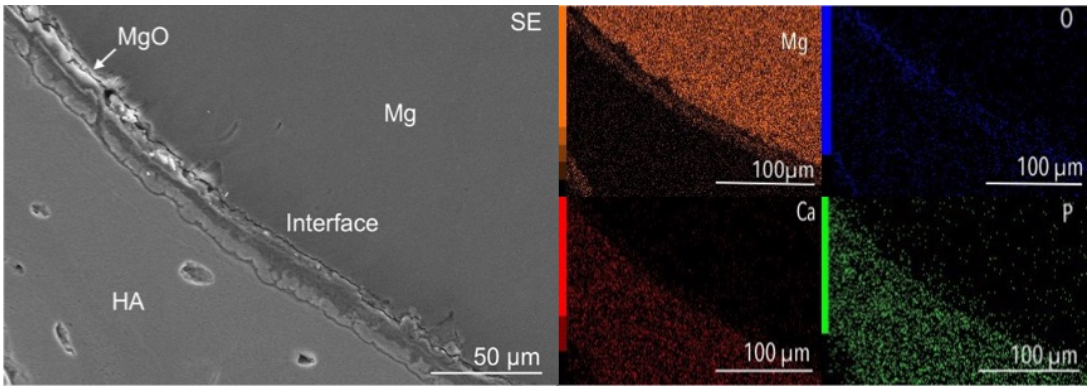

Figure 1. *SEM and EDS analyses of Mg/HA composites*

The density of the composite was approximately 5 % higher than Mg and 14 % lower than HA, obtaining a lightweight composite in the range of cancellous bone density. The hardness values of the composite were 14 % higher than Mg and 11 % lower than the hardness but brittle HA. On the other hand, the Mg/HA composite shows an extreme improvement in the values of yield strength (YS 470 %) and in the ultimate compressive strength (UCS 748 %) compared to the original porous HA ceramic scaffold (Figure 2). The interpenetration of the Mg stabilizes the ceramic struts and partially prevents strut bending, resulting in a significant improvement in the mechanical properties of the ceramic scaffold. However, the resulting Mg/HA composite indicates inferior mechanical property values (42 % YS and 22 % UCS) compared to the bulk Mg, probably due to the formation of a thick layer of MgO. The thickness of the layer could provide poor interfacial bonding between the HA scaffold and the metal matrix, so load cannot be transferred effectively from the matrix to the scaffold, which leads to lower strength and earlier failure. The failure in composites was correlated with particle agglomerations; techniques such as power metallurgy reported composites with 30% reinforcement, which have 72 MPa and 92 MPa of yield and compressive strength, respectively **[8]**. These values are lower than those obtained for Mg/HA interpenetrating composites with a smaller fraction of Mg (~20%), 10% YS, and 34% UCS, respectively. Therefore, the infiltration technique is one of the best techniques to produce metallic composites with free selection of reinforcement (i.e., geometry, size, structure, etc.) and matrix. In addition, incorporating a natural scaffold could help design composites with properties (solubility, stability, microstructure, mechanical properties, etc.) closer to those of the natural constituent.

In future work, in principle, MgO formation should be avoided or highly minimized by applying a treatment to the scaffold before infiltration to further improve the mechanical properties of Mg/HA composites.

Acknowledgments
The authors would like to acknowledge the financial support from DGAPA-PAPIIT UNAM IN102422 for funding the project. IAFV would like to acknowledge C. Flores, G. A. Lara-Rodríguez, C. Ramos, O. Novelo, A. Tejeda, R. Reyes, A. Lopez V., F. Garcia, E. Hernández-Mecinas, A. Bobadilla, J. Romero and E. Reyes-Morales for their technical support. "Por mi raza hablará el espíritu".

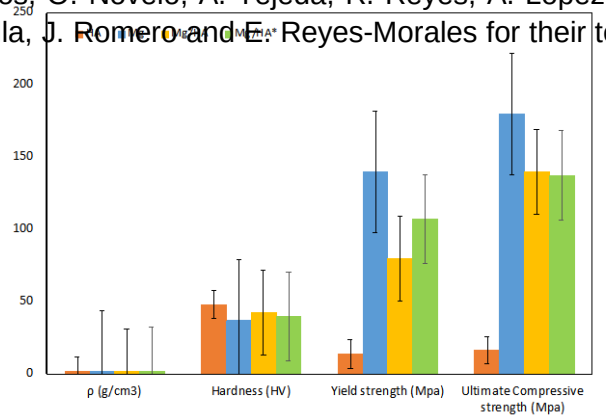

Figure 2. *Density and Mechanical Properties of Mg, HA, and Mg/HA composite. The Mg/HA* values were calculated using the mixing rules.*

Conclusions

The Mg-HA biocomposite was successfully fabricated using a liquid metal infiltration technique and incorporating a natural scaffold as a reinforcement. A high densification was achieved, reducing pores or voids (down to 1%) in the composite. The microstructural analyses showed that a ticker layer of MgO was localized between the matrix and the reinforcement due to the organic matter that reacts with liquid Mg. The mechanical properties of the Mg-HA biocomposite are probably affected by the MgO layer; UCS decreased by 22% compared with Mg. With the results presented in this study, the production of continuous Mg/HA composites incorporating a natural scaffold as reinforcement could be a milestone for employment as biodegradable metal composites for hard tissue scaffolds.

References

[1] Wang, X., Li, J., Xie, M., Qu, L., Zhang, P., & Li, X. Mater. Sci. Eng., C **(2015)**., 56, 386-392.
[2] Salernitano, E., & Migliaresi, C. J. Appl. Biomater. Biomech. **(2003)**, 1, 13-8.
[3] Know, S., Jun, Y., Hong, S., & Kim, H. J Eur Ceram Soc **(2003)**, 23, 1039-45.
[4] Wang, X., Zhang, P., Dong, L., Ma, X., Li, J., & Zheng, Y. Mater Des **(2014)**., 54, 995-1001.
[5] Ma, X., Dong, L., & Wang, X. Mater Sci Eng C Mater Biol Appl **(2013)**., 33(7), 4266-73.
[6] Wang, X., Nie, Q., Ma, X., Fan, J., Yan, T., & Li, X. Transactions of Nonferrous Metals Society of China, (2017). 27(9), 1996-2006.
[7] Escalera, C.H.; Figueroa, I.A.; Casas-Luna, M.; Rodríguez-Gómez, F.J.; Piña-Barba, C.; Montufar, E.B.; Čelko, L. J. Compos. Sci. **(2023)**, 7, 467.
[8] X. Gu, W. Zhou, Y. Zheng, L. Dong, Y. Xi, D. Chai, Mater. Sci. Eng. C 30 **(2010)**, 827–832.

Acknowledgments
The authors would like to acknowledge the financial support from DGAPA-PAPIIT UNAM IN102422 for funding the project. IAFV would like to acknowledge C. Flores, G. A. Lara-Rodríguez, C. Ramos, O. Novelo, A. Tejeda, R. Reyes, A. Lopez V., F. Garcia, E. Hernández-Mecinas, A. Bobadilla, J. Romero and E. Reyes-Morales for their technical support. "Por mi raza hablará el espíritu".

“Transmission loss study dependent on thermal aging for Polymer Optical Fibers.”

González-Trueba L.H.[1], Grabski V.[1], L. Alexandrova[2], Gabriel Torres Villaseñor[2]

[1]Instituto de Física, UNAM, gonzalez.lh@gmail.com
[2]Instituto de Ingeniería de Materiales

Abstract

The aging of polymeric optical fibers was studied, subjecting them to a temperature of 80°C. The relative loss of transmission due to thermo-oxidative aging and with respect to the mechanical stress generated by different curvatures was measured. The maximum transmission loss was 15% up to 432 hours, where the highest amount of loss was obtained in the first 72 hours. So far it has been shown that with small diameter curves, there is less transmission loss than with those with a larger curvature diameter.

Introduction

The aging of materials is studied in various areas to predict their lifetime. In this work, the aging of polymeric optical fibers (POFs) for use in radiation detectors is analyzed, due to environmental factors [1] and mechanical stresses. The POFs that were studied were used in the FV0 detector, for the ALICE experiment at the LHC at the CERN. The interest in this study is that the FV0 detector consists of 50 thousand optical fibers arranged at curvatures generated by the design and space limitations for the detector [2]. It is of interest to estimate possible fiber degradations considering design-specific conditions during the next 10 years.

Since thermal energy has been used to generate changes in the material and accelerate its aging, the Arrhenius equation has been used to calculate the aging acceleration factor for 80°C. The acceleration factor is 277.9, so with this factor, the exposure time equivalent to 10 years is about 432 hours. The estimated activation energy for POF aging is 0.84 eV for a temperature of 80°C [3,4].

Complementary studies were conducted to understand the causes of transmission loss after aging. Mechanical tests, x-ray diffraction, and infrared spectroscopy (FTIR) were carried out.

Experimental Methodology

The POFs that were used in the detector are Asahi, Model SB-1000 [1], with a diameter of 1mm. This POF is composed of a core of poly methyl methacrylate (PMMA) and a cladding of a fluoropolymer. One meter-long fibers were assembled and FC-type connectors were placed in each terminal face. A 405 nm wavelength Picosecond Laser System, model PiL040X was used, which was connected to a commercial light splitter, each fiber of the splitter has a diameter of 100µm. Two channels of the splitter were used, one of them SP1 was connected

to a photomultiplier tube (PMT) as a reference and the other channel of the splitter SP11 was connected to the fiber, which was coupled to another PMT, see Figure 1. Both PMTs are Hamamatsu Model R5946-70. The fibers were subjected to curvatures of 50, 70, 100, and 200 mm in diameter. Transmission was measured before and after aging.

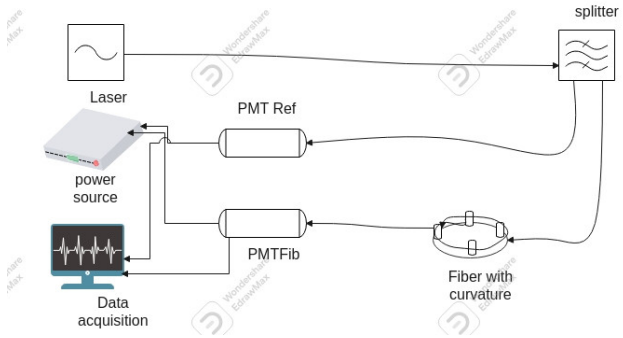

Figure 1. Experimental setup, the fiber connections are shown for measuring transmission loss, using photomultiplier tubes.

In the tensile tests, three different times of aging were analyzed, 0, 72, and 432 hours. Three fibers were studied for each aging. A universal tensioning machine Instron 1125 with a strain speed of 10 mm/min was used.

To obtain the diffractograms, three different samples were studied, the complete fiber, the fiber core, and the coating. Once the samples were obtained, they were ground and analyzed with RX with a wavelength of 1.56 Å. In the same way, FTIR spectra were obtained with a spectrometer Nicolet 510P.

Results

For transmission measurements, fibers with different curvatures were compared by heating them to 80°C every 72 hours. In Figure 2, the first 72 hours are those that show the most obvious change in the transmission. So far it has been observed that fibers with smaller curvatures, 50 and 70 mm, have between 5 and 7% transmission loss, and those with larger diameters 100 and 200 mm have between 11 and 13%. After heating probably some recovery of mechanical micro damages for the small curvatures. Figure 2 also shows the stability of the measurements that have a 1.2% sigma.

For the mechanical tests, Young's modulus of each aging was obtained and on average the more the material ages, the modulus decreases, so a material with lower rigidity is obtained [7], Figure 3.

In the RX diffractograms, it is observed that in the cladding, the reflections show a decrease in broadening that indicates a greater crystallinity of the sample [7]. For the nucleus, we did not observe any change in the diffractograms, Figure 4.

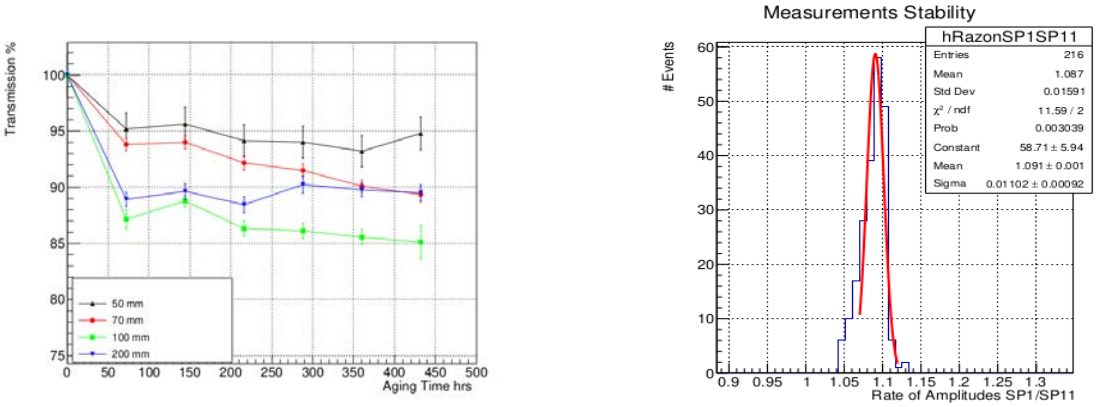

Figure 2. In left figure shows the relative transmission is dependent on aging time and bending diameter. The right figure shows the stability of the measurements with a 1.2% on the sigma.

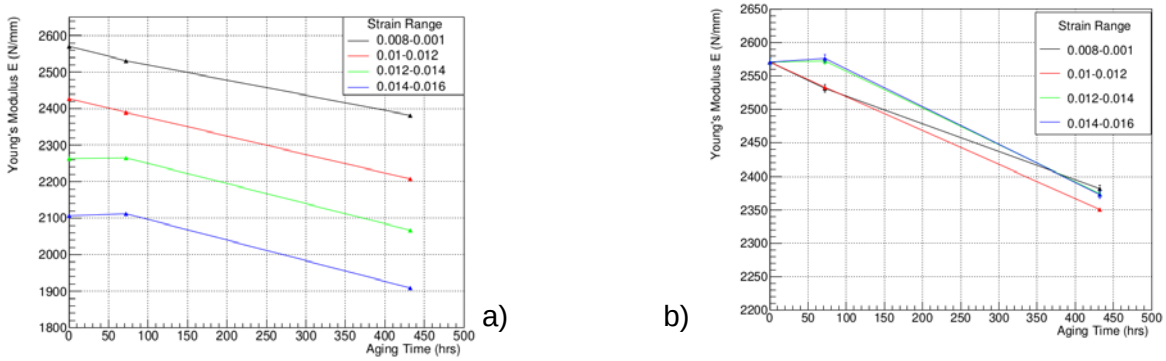

Figure 3. a) Young´s Modulus changing with the time of aging in different strain ranges, b) Normalized Young´s Modulus from graph a).

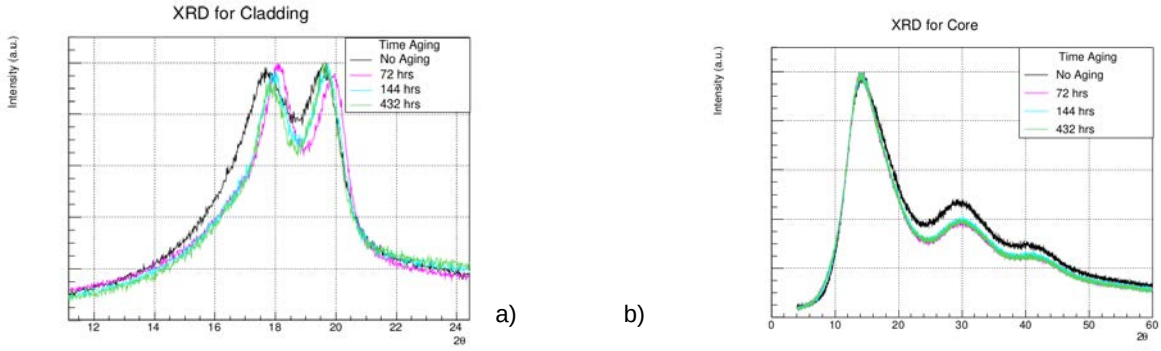

Figure 4. a) Cladding x-ray diffraction normalized; it shows the difference in the width with respect to the non-aging sample. b) Zoom of the first two peaks, which shows the change of the angle 2θ in each aging.

In the infrared spectrometry, no change was found between different aging times, however, it was compared with the OMNIC software database, and a 70% coincidence with fluorinated polyvinylidene (PVDF) was found. Therefore, both the diffractograms and the infrared spectra coincide with this polymer [5,6].

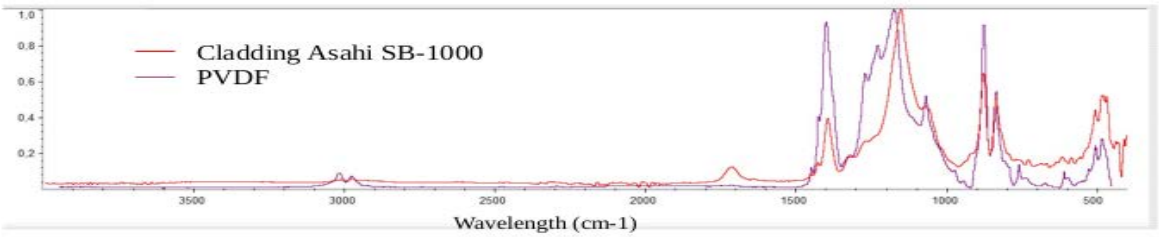

Figure 9. FTIR for cladding shows a match with polyvinylidene fluoride of 69.98%

Conclusions

Significant changes are observed in the first 72 hours of aging, for the 50 mm fiber there is a loss of 5%, for the 70 mm there is a loss of 7%, the 100 mm shows a loss of 13%, and the 200 mm there is a loss of 11%. So far it has been shown that with small diameter curves, there is less transmission loss than with those with a larger curvature diameter. The maximum loss for 432 hours is 15%. Tensile tests indicate that there is a decrease in Young's modulus as aging increases by 10%. Likewise, a change is seen in the diffractograms of the cladding that indicate that the material is more crystalline because its chains are rearranged, this can cause a change in its optical properties. From the IR spectrum, it is concluded that the coating material may be PVDF or some mixture with it.

Reference

[1] Anilkumar Appajaiah, H-J. Kretzschmar, W. Daum Aging behavior of polymer optical fibers: Degradation characterization. J. Applied Polymer Sciences, DOI 10.1002/app.25214, **2006**.
[2] V. Grabski, arXiv:1909.01184. Cornell Univ.,**2019**.
[3] Wenhua Yin. Aging behavior and lifetime prediction of PMMA under tensile stress and liquid scintillator conditions, Adv. Ind. Eng. Polym. Res**.** V.2 (pp. 82-87) **2019**.
[4] J.Janting, J.Grundtvig Theander, H. Egesborg On Thermal Acceleration of Medical Device Polymer Aging. IEEE Transactions on Device and Materials Reliability, VOL. 19, NO. 2, 313-321 **2019.**
[5] Ruggiero E., Reboredo M., Castro M. Structural and dielectric properties of hot-pressed poly(vinylidene fluoride)-based composites. J. Compos. Mater. **2018**;52(10):1399-1412.
[6] Reis Medeiros K.A. Evaluation of the electromechanical behavior of polyvinylidene fluoride used as a component of risers in the offshore oil industry. Oil Gas Sci. Technol. 73, (pp. 48) **2018.**
[7] Askeland D. The Science and Engineering of Materials 3rd Ed. (pp. 462) **1998.**

Acknowledgments

Quím. Miguel Ángel Canseco Martínez - Laboratorio de Espectroscopia IIM-UNAM. Dra. Daniella Reggio Laboratorio Nacional para la investigación y la conservación del patrimonio cultural LANCIC-IFUNAM. M. en C. Eliezer Hernández Mecinas - Laboratorio de Pruebas Mecánicas. Dr. Luis Manuel Montano Zetina - Departamento de Física -CINVESTAV. M. en C. César Ruiz Trejo, M. en C. Eduardo López Pineda - Laboratorio de Dosimetría, IFUNAM. Tec. Antonio Morales Espino- Laboratorio de Refinamiento de Estructuras Cristalinas. Aarón Ramírez Torres, Joel Itauqui Osornio Martínez - Taller mecánico IFUNAM. Francisco Márquez Torres - Diseño IFUNAM.

Polymat Contributions

Study of the lability in the thermal properties of carbohydrates non-digestible of low molecular weight

Mayte López-Tapia[1], Emma Gloria Ramos-Ramírez[1], Alfredo Cruz-Orea[2], and Juan Alfredo Salazar-Montoya[1].

[1]Biotechnology and Bioengineering Department. [2] Physic Department. CINVESTAV-IPN. Av. Instituto Politécnico Nacional 2508, Col. San Pedro Zacatenco, México City. 07360. Email: jsalazar@cinvestav.mx

Introduction

Food products that include non-digestible carbohydrates (NDC) in their formulations present an increase in their prebiotic properties. Within the NDC we have fructooligosaccharides (FOS), agave fructans (ADF), and polydextrose (PDX). However, some of the food manufacturing processes involve heat treatments that produce physical and chemical changes in the NDCs. Therefore, it is necessary to determine the NDC's thermal properties, such as diffusivity, effusivity, and thermal conductivity.

There are several techniques to determine the thermal properties, one of them is the photothermal ones that are based on the detection of the thermal waves produced by the absorption of a light beam; that is, by photon absorption [1,2]. These techniques include photopyroelectric (PPE) and open photoacoustic cell (OPC).

Considering the importance of thermal properties, this study aims to determine the effusivity, diffusivity, and thermal conductivity of fructose, sucrose, FOS, ADF, and PDX using photothermal techniques.

Materials and methods

To carry out this study, we used digestible carbohydrates: D-Fructose (Sigma Aldrich, USA) and sucrose (Mallinckrodt, Chemical, USA); as well as non-digestible carbohydrates: Fructooligosaccharides (FOS) (Nutraflora® P-95, Ingredion, Mexico), agave fructans (ADF) (Bioagave®, Ingredion, Mexico) and, Polydextrose (PDX) (Polidex® Fiber Type II, Ingredion, Mexico).

Open photoacoustic cell (OPC) was used to determine thermal diffusivity, with the methodology of Alvarado-Noguez, et al. [3]. An argon laser was employed, whose light beam is mechanically modulated with the help of a chopper, using a variable frequency from 10 to 110 Hz. The output signal produced by the microphone is analyzed using a lock-in amplifier and the data obtained are stored on a computer.

Thermal diffusivity was determined using the photopyroelectric technique in reverse configuration (IPPE) technique. According to the methodologies reported by Flores-Cuautle, et al. [4] and Alvarado-Noguez, et al. [3]. Subsequently, the signal is treated with a lock-in amplifier and the amplitude and phase are determinated as a function of the modulation frequency (f).

For its part, the thermal conductivity was calculated from the thermal effusivity and diffusivity using Equation 1

$$\kappa_s = e_s\sqrt{\alpha_s} \qquad \text{Equation 1.}$$

Where e_s is the thermal effusivity $\left(\frac{J}{m^2K}\sqrt{\frac{1}{s}}\right)$, κ_s is the thermal conductivity (W m^{-1} K^{-1}), α_s is the thermal diffusivity (m^2/s) and ρ is the density (kg m^{-3}).

Results and discussion

From the experimentation performed, we had it was obtained that the value of thermal effusivity for the carbohydrates studied is between 7.344 y 3.270 $\frac{W\sqrt{s}}{m^2K}$ (Table 1). These values are like those reported for turmeric (*Curcuma longa*), a spice composed mainly of carbohydrates such as starch [5], whose thermal effusivity is between 518.7 y 539 $\frac{W\sqrt{s}}{m^2K}$ [3].

Table 1 Diffusivity, effusivity and thermal conductivity of the studied carbohydrates.

Oligosacárido funcional	$\boldsymbol{\alpha}$ ($\times \mathbf{10^{-7}}$ m^2 s^{-1})	$\boldsymbol{e_s}\left(\frac{W\sqrt{s}}{m^2K}\right)$	$\boldsymbol{\kappa_s}\left(\frac{W}{m\,K}\right)$
Fructose	5.857±0.640	507.35±17.93	0.388
Sucrose	4.582±0.685	421.96±7.42	0.286
Fructooligosaccharides	5.005±0.686	413.94±67.9	0.293
Agave fructans	7.344±1.464	433.54±36.43	0.372
Polydextrose	3.270±0.522	515.89±26.93	0.295

$\boldsymbol{\alpha}$, is the thermal diffusivity of the sample; $\boldsymbol{e_s}$ is the thermal diffusivity of the sample; $\boldsymbol{\kappa}$, is the thermal conductivity.

The values obtained for the thermal diffusivity (Table 1) are also close to those reported for other carbohydrates and biological samples such as amylose, amylopectin, corn starch, and turmeric, whose diffusivities are in a range between 3.12 y 7.5 × 10^{-7} m^2 s^{-1} [3,6–8].

Both thermal techniques are related to heat diffusion, nevertheless, thermal diffusivity is related to the rate of heat flow through a body, making it a volume property, and thermal effusivity is related to heat exchange at the surface level [9,10]. Polydextrose has a low heat penetration, compared to the other carbohydrates studied, but heat transfer at the surface level is fast. Polydextrose has a complex and compact structure [11] that probably hinders molecular movement, thus affecting heat diffusion through the tablet. On the other hand, ADFs have the highest thermal diffusion value of all carbohydrates, it is likely that this also originates from its structure, as it is formed by fructose units linked together by an oxygen atom, which gives it greater flexibility [12].

In another way, although it is known that heat diffusion is a phenomenon that occurs in all three spatial dimensions, the mathematical model used to determine thermal diffusivity is one-dimensional. The one-dimensional analysis considers that materials with homogeneous

behavior present an excitation phase and subsequently have a period in which the heat flow normal to the illuminated surface predominates [10].

Furthermore, this model is only applicable to thermally thick samples, which implies that the heat gradient along the sample is significant; that is, the sample easily absorbs the thermal energy at the surface and does not easily transfer it through the sample, so the temperature where the light beam strikes decays by more than 63%. Considering this, there may be significant fluctuations in the value of thermal diffusivity as a function of the thickness of the sample.

It is necessary to consider the relevance of the correct measurement of thermal effusivity and diffusivity; since the values of both thermal properties are required for the calculation of thermal conductivity, it is likely that they have influenced the values obtained, which are between 0.286 y 0.372 $\frac{W}{m\,K}$, values higher than those reported for sugars such as sucrose (0.085-0.167$\frac{W}{m\,K}$) [13] and polysaccharides such as starch (0.065-0.220 $\frac{W}{m\,K}$) [14].

However, other factors may influence the values obtained from the thermal properties, such as the moisture content, the interstitial air in the carbohydrate tablets, the level of cohesion between the particles, and the size, and distribution of the particles.

Conclusions

It can be concluded that the thermal properties of the studied NDCs are within the range of values reported in the literature for other biological compounds and the thermal diffusivity values of ADF and PDX may depend on the flexibility of their structure. Finally, it was observed that the thickness of the tablets affects the applicability of the mathematical model of thermal diffusivity.

References

(1) Zapata, E.; Emiliano, C.; Orizaba, Z. Introducción Técnicas Fototérmicas. *UTCJ Theorema* **2020**, 202–209.

(2) Massot-Pérez, M. Desarrollo y Aplicación de La Calorimetría Fotopiroeléctrica al Estudio de Transiciones de Fase, Universidad del País Vasco, **2008**.

(3) Alvarado-Noguez, M. L.; Hernández-Aguilar, C.; Domínguez-Pacheco, F. A.; Cruz-Orea, A.; Sánchez-Sinéncio, F. Photothermal Techniques Applied to the Thermal and Optical Characterization of Curcuma Longa. *Int J Thermophys* **2018**, *39* (8). https://doi.org/10.1007/s10765-018-2418-8.

(4) Flores-Cuautle, J. J. A.; Cruz-Orea, A.; Suaste-Gomez, E. Thermal Effusivity of the Pb0.88Ln0.08Ti 0.98Mn0.02O3 (Ln=La, Eu) Ferroelectric Ceramic System by Inverse Photopyroelectric Technique. *Ferroelectrics* **2009**, *386* (1), 36–40. https://doi.org/10.1080/00150190902961264.

(5) United States Department of Agriculture. *FoodData Central*. FoodData Central Spices, turmeric, ground. https://fdc.nal.usda.gov/fdc-app.html#/food-details/172231/nutrients (accessed 2022-04-03).

(6) Fernández-Muñoz, L. J.; Zelaya-Angel, O.; Cruz-Orea, A.; Sánchez-Sinencio, F. Phase Transitions in Amylose and Amylopectin under the Influence of Ca(OH)2 in Aqueous Solution.

Anal. Sci. **2001**, *17 Special* (1), s308–s341. https://doi.org/http://doi.org/10.14891/analscisp.17icpp.0.s338.0.
(7) Mohos, F. Á. Engineering Properties of Foods. In *Confectionery and Chocolate Engineering*; Wiley-Blackwell: Oxford, UK, **2010**; pp 52–96. https://doi.org/10.1002/9781444320527.
(8) Fellows, P. J. Heat Processing. *Food Processing Technology* **2009**, *2*, 339–366. https://doi.org/10.1533/9781845696344.3.339.
(9) Dante, R. C.; Dante, R. C. Metals. In *Handbook of Friction Materials and their Applications*; **2016**; pp 123–134. https://doi.org/10.1016/B978-0-08-100619-1.00009-2.
(10) Rajic, N. *Non-Destructive Evaluation (NDE) of Aerospace Composites: Flaw Characterisation*; **2013**. https://doi.org/10.1533/9780857093554.3.335.
(11) Câmara, A. K. F. I.; Paglarini, C. de S.; Vidal, V. A. S.; dos Santos, M.; Pollonio, M. A. R. Meat Products as Prebiotic Food Carrier. In *Adv. Food Nutr. Res.*; Academic Press Inc., **2020**; Vol. 94, pp 223–265. https://doi.org/10.1016/bs.afnr.2020.06.009.
(12) Barclay, T.; Ginic-Markovic, M.; Cooper, P.; Petrovsky, N. Inulin - A Versatile Polysaccharide with Multiple Pharmaceutical and Food Chemical Uses. *J. Excipients Food Chem.* **2010**, *1* (3), 27–50.
(13) Maccarthy, D. A.; Fabre, N. Food Properties and Computer-Aided Engineering of Food Processing Systems. In *Food Properties and Computer-Aided Engineering of Food Processing Systems*; Singh, R. P., Medina, A. G., Eds.; Springer Netherlands: Dordrecht, **1989**; pp 105–111. https://doi.org/10.1007/978-94-009-2370-6.
(14) Drouzas, A. E.; Saravacos, G. D. Effective Thermal Conductivity of Granular Starch Materials. *J Food Sci* **1988**, *53* (6), 1795–1799. https://doi.org/10.1111/j.1365-2621.1988.tb07845.x.

Acknowledgements
The authors gratefully the technical support of the Eng. María Dolores Díaz Cervantes, Research Assistant of the Biotechnology and Bioengineering Department of CINVESTAV-IPN.

SYNTHESIS AND CHARACTERIZATION OF SURFACTANT-MODIFIED CHITOSAN FOR THE PREPARATION OF DRUG DELIVERY NANOCARRIERS

H. Iván Meléndez-Ortiz[1], Lariza Sánchez-Salazar[2], Gladis Cortéz-Mazatán, Bertha Puente-Urbina[2], René D. Peralta-Rodríguez[2]

[1]CONACyT-Centro de Investigación en Química Aplicada, Blvd. Enrique Reyna Hermosillo #140, 25294, Saltillo, Coahuila, Mexico, Email: hector.melendez@ciga.edu.mx
[2]Centro de Investigación en Química Aplicada, Blvd. Enrique Reyna Hermosillo #140, 25294, Saltillo, Coahuila, Mexico

1.1 Introduction

Chitosan (CS), a nature-derived polysaccharide, is a promising nano-carrier material with good biocompatibility and biodegradability [1, 2]. However, the biomedical applications of CS are restricted because of its poor aqueous solubility in neutral/alkaline aqueous solutions. CS can be modified by grafting functional molecules taking advantage of the hydroxyl and amine groups in its structure, improving its aqueous solubility and endowing it with amphiphilic and specific biological properties [3, 4].

In this work, CS was modified with the non-ionic surfactant Brij-35 with various grafting degrees. First, Brij-35 was mofidied with succinic anhydride (SA) to give Brij-SA which was subsequently reacted with CS through an amidation reaction to obtain the Brij-grafted chitosan copolymers (CS-Brij35). The CS-Brij35 copolymers were characterized by infrared spectroscopy (FT-IR) and nuclear magnetic resonance (NMR). The obtained CS copolymers showed the ability to form self-assembled nanostructures which could be useful for the development of hydrophobic drug nano-carriers.

2.2 Materials and Methods

2.1 Materials

Chitosan (molecular weight 50,000 -190,000 Da, 75–85 % deacetylated), Brij-35, succinic anhidride (SA), 4-dimethylamino pyridine (DMAP), N-(3-dimethylaminopropyl)-N′-ethylcarbodiimide hydrochloride (EDC), and anhydrous dichloromethane (DCM), were purchased from Sigma Aldrich.

2.2 Functionalization of Brij-35 with SA

A mixture containing 1.15 g of Brij-35 and DMAP (0.12 g) in DCM (20 mL) was reacted with SA (0.1 g) for 24 h under N_2 atmosphere. Once the reaction was completed, the mixture was washed with aqueous HCl solution (10%, v/v) and the organic solution was collected. The Brij-SA was obtained by evaporating the organic solvent under reduced pressure. A schematic representation of this reaction is shown in figure 1.

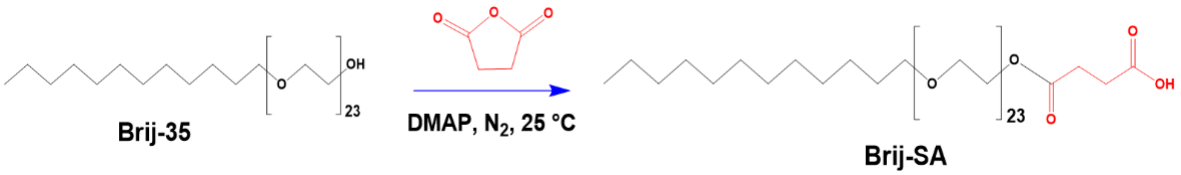

Figure 1. Chemical reaction of Brij-35 with SA.

2.3 Grafting of Brij-SA onto CS

For the grafting of this non-ionic surfactant onto CS, firstly Brij-SA (1.29 g) was activated with EDC (1.2 mmol, 0.23 g) using 5 mL of DCM as solvent for 24 h at 25 °C. The activated Brij-SA was added into CS acetic acid solution (1%, v/v, pH 4) and reacted at 25 °C for 24 h. Subsequently, the reaction was terminated by dialyzing against distilled water and the samples were lyophilized. Brij-grafted chitosan copolymers (CS-Brij35) with different grafting yields were synthesized using different Brij-SA:CS molar ratios (1:3 1:7, 1:14, 1:29 y 1:60) (Table 1). The grafting degree (GD) of CS-Brij35 copolymers was calculated by using the integrated peak areas at 1.05 (Brij-SA) and 3.2 ppm (CS).

3. Results and discussion

3.1 Functionalization of Brij-35 with SA

The ^{1}H NMR spectrum of Brij-SA is shown in Fig. 2a. Brij-35 showed characterisitic signals at 3.4 and 1.05 ppm due to (-C**H**$_2$O) and –C**H**$_3$, respectively. The modification of Brij-35 with SA was confirmed by the new signal at 2.7 ppm in the spectrum of Brij-SA which was due to the succinoyl methylenes. In addition, the FTIR spectrum of Brij-SA showed the signal of C=O from SA (Fig. 2b).

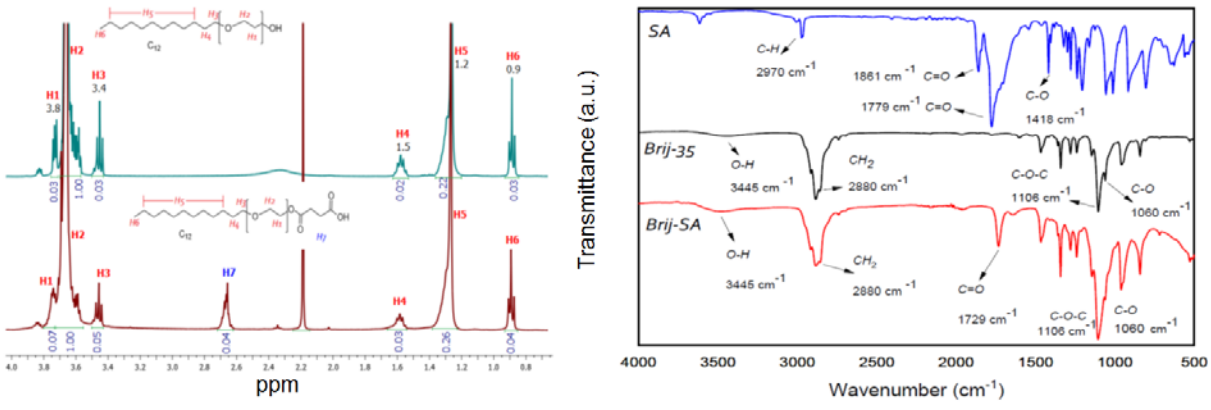

Figure 2. a) NMR and b) FTIR spectra of Brij-35 and Brij-SA.

3.2 Grafting of Brij-SA onto CS

An schematic representation of the grafting of Brij-SA onto CS is shown in figure 3. Grafting of Brij-SA onto CS was carried out at different Brij-SA:CS molar ratios and the obtained grafting

yields are shown in Table 1. It can be seen that as the initial amount of CS increased, the grafting yield was reduced. Also, the values of grafting yield agree with the theoretical ones.

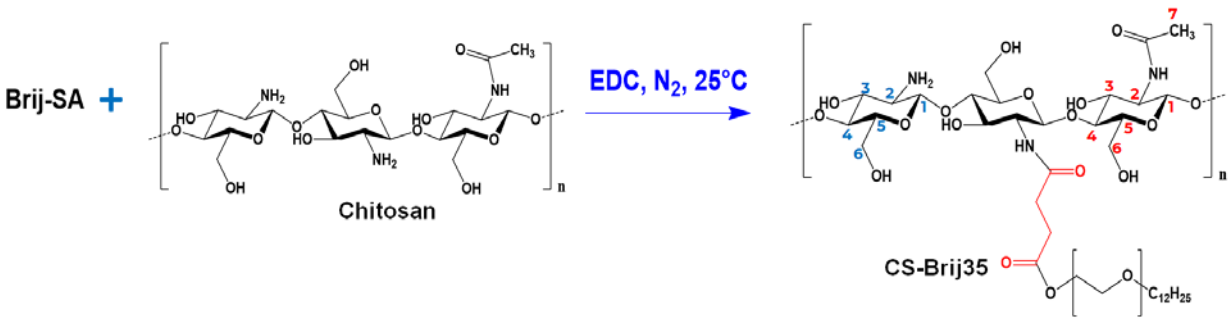

Figure 3. Chemical reaction of Brij-SA with chitosan to obtain CS-Brij35 copolymers.

Table 1. Obtained grafting yields of Brij-SA onto CS at differente molar ratio Brij-SA:CS.

Molar ratio Brij-SA:CS	Theoretical grafting degree (%)	Average grafting degree (%)
1:3	44	47 (± 3.6)
1:7	19	22 (± 2)
1:14	9	9 (± 0.3)
1:29	4	7 (± 2.6)
1:60	2	4 (± 2.6)

On the other hand, the ^{1}H NMR spectra for these copolymers are shown in figure 4a. The spectrum of pristine CS showed signals at 1.9 ppm due to the methyl group from the acetylated glucosamine units (H7), as well as a signal at 3.2 ppm for the proton (H2) of the glucosamine units. Also, it exhibited signals in the range of 3.5-3.9 due to the protons of the glucose rings (H3-H6). For their part, the spectra of the synthesized Brij-modified CS copolymers exhibited a signal at 1.1 ppm from the methyl protons of the long-chain alkyl group of Brij-35 which confirms their modification. In addition, the FTIR spectra of these copolymers showed a signal at 1541 cm^{-1}, due to the N-H bending from the formed amide by by the reaction between the amine and acid groups from CS and Brij-SA respectively (Fig. 4b).

Finally, the critical micelle concentration (CMC) of the CS-Brij35 synthesized with a molar ratio of 1:7 was determined by different techniques (surface tension, density, conductivity, and pH). The results showed CMC values in the interval of 0.1-0.2 mg/mL which make it suitable as nanocarrier for development of drug delivery systems.

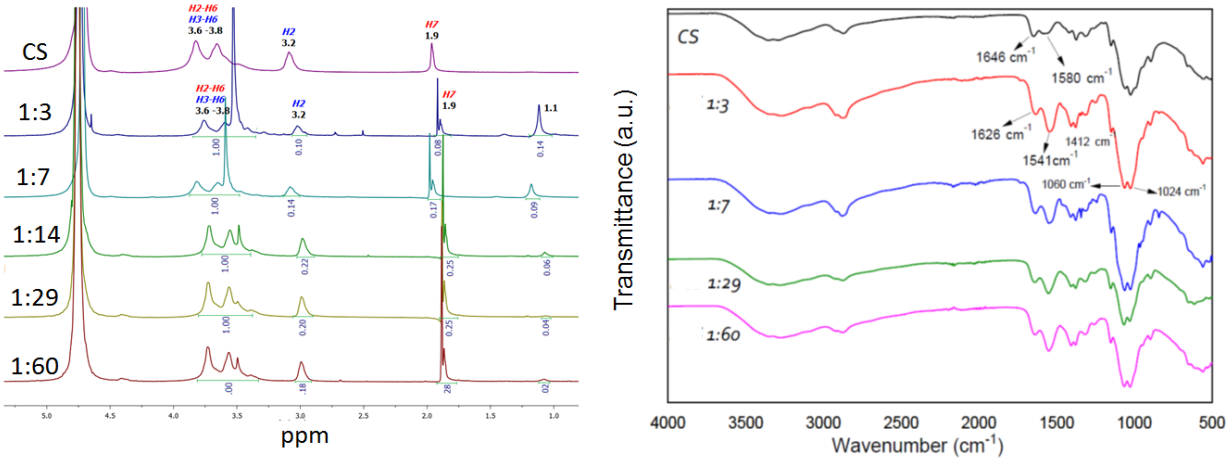

Figure 4. a) NMR and b) FTIR spectra of the CS copolymers synthesized with different Brij-SA:CS molar ratios.

Conclusions

CS-Brij35 copolymers with various grafting yields were synthesized for the first time. Grafting was confirmed by ^{1}H NMR and FTIR characterizations and it was dependent of the Brij-SA:CS molar ratio. Some physicochemical properties of the pristine CS were modified by the functionalization with Brij-35. The appropriate CMC of the CS-Brij35 copolymers endows the capability of CS derivatives to self-assemble into nanocarriers for drug delivery.

References

[1] Int J Biol Macromol. **2019**, 126, 517–24.
[2] Int. J. Biol. Macromol. **2018**, 109, 273–286.
[3] Carbohydr. Polym. **2019**, 204, 89-96.
[4] Drug Dev. Ind. Pharm. **2018**, 44, 1273–84.

Acknowledgements

The authors acknowledge financial support from CONAHCYT through Laboratorio Nacional de Micro y Nanofluídica, Subsede CIQA (Projects 299058, 2019 and 314907, 2020) and Project No. A1-S-46343 CB 2017-2018. Author Meléndez-Ortiz is grateful to the program “Investigadoras e Investigadores por México-CONACyT”.

"Biosynthesis and characterization of Ag and Ti nanoparticles through - *Chamaemelum nobile* and *Mentha piperita*"

***Salomón Alberto Mondragón Román*[1], *Sonia Martínez-Gallegos*[1], *Javier Illescas*[1], *José Luis García*[1], *Pablo Schabes-Retchkiman*[2].**

[1]*Tecnologico Nacional de México / Instituto Tecnológico de Toluca, División de Estudios de Posgrado e Investigación, México*
[2]*Universidad Nacional Autónoma de México, Instituto de Física, México*

Abstract

The size of metallic nanoparticles are equal or lesser to 100 nanometers as follows biosynthesis method; this size makes them have improved microbiological caracteristics by the increment of the superficial area. Environmental friendly methods for synthesis of metallic nanoparticles like bioreduction uses biomolecules from plants such as polyphenols and terpenoids, among others, to reduce a metallic salt. In this work chamomile (*Chamaemelum nobil*e) and mint (*Mentha piperita*) were used to obtain Ag and Ti nanoparticles. Ag and Ti nanoparticles solution were characterized by UV-Vis, FTIR and TEM. The results obtained shows a color shift in the aqueus solution, brownish for Ag and pale yellow for Ti nanoparticles, UV-Vis technique show the resonance plasmon for each metallic nanoparticle, FT-IR shows the characteristic vibrations associated with functional groups related to the organic matter in the plants, the TEM shows different sizes and diameter of nanoparticle, we also evaluate which of the two plants confers a higher bactericidal capacity to Ag and Ti nanoparticles.

Introduction

Nanotechnology is the science responsible for the research, production and development of materials with dimensions between 1 and 100 nm; due to their size, they share characteristics between the quantum and physical worlds, which together with the increase in the surface area of nanomaterials, allow for improvements in their characteristics [1].

Green synthesis methods are environmentally friendly and have become increasingly popular in chemistry (Fahmy et al., 2020); the need to find processes that consume less energy, resources or are less polluting has driven the scientific community to find new methodologies. Specifically in the production of nanoparticles, "green" methods of synthesis help to eliminate the use of reductants that generate hazardous waste, which are very expensive and ecologically incompatible reagents due to the polluting waste they produce [2].

Phytosynthesis of nanoparticles, consists of taking advantage of existing biomolecules in plants as reducing and stabilizing agents [3]; the advantages provided by the use of plants to create extracts for the phytosynthesis process are the ease of access to plants, safety of handling, as well as the fact that they possess a large amount of active agents that promote the reduction of metal ions.

Experimental

Twenty mature plants of Chamaemelum nobile (chamomile) and twenty more of *Mentha piperita* (mint) were obtained from orchard, the selection of mature plants was made to check the concentration of total polyphenols at the mature stage.

The biomass was left to dry at room temperature on a layer of paper in a dark room for 30 days. Subsequently, the leaves of the plants were sectioned and placed in a Riossa H-33 drying oven, spread on aluminum foil, at a temperature of 50 °C +-5 °C for 24 h. The leaves of the plants were crushed and dried in an oven.

The dried plant leaves were crushed in an agate mortar and sieved at 100 mesh (149 µm) until a fine powder was obtained. 100 mL of solutions of $AgNO_3$ at 0.1 M and TiO_2 at 0.1 M were prepared with deionized water. The pH was obtained with a Hanna HI98130 portable potentiometer, calibrated with buffer solutions pH 7 JT5608-1 and pH 4 JT5606-1 from JT Baker. Subsequently, the pH of each metal solution was modified to pH 4 using a 0.15 M HNO_3 solution.

An 80% v/v ethanol-water solution was prepared; 25 mL of this solution was used, to which 125 mg of powder of each of the biomasses were added separately. Each of the mixtures was left to stand for 15 min at 4 ºC in the dark; the green extract obtained was filtered with a 0.45 µm nitrocellulose membrane (Whatman).

Equal volumes of each of the metal solutions and plant extract (5:5 mL) were mixed in 15 mL polypropylene tubes. Once mixed, the 4 tubes with solution were placed inside the ultrasonic bath for 15 min at 20 °C; once the time was over, they were left to rest for 5 min more. Finally, the polypropylene tubes were centrifuged again at 5000 rpm for 20 min.

The samples were separated by decantation; on the one hand, the supernatant remained and on the other, the precipitate, the latter was destined for confinement and the supernatant was kept refrigerated at 4 °C in amber bottles for subsequent characterization.

The optical response of the Ag and Ti metals of the nanoparticles was performed by UV-Vis scanning in the range of 200 to 900 nm (λ), using the UV-Vis spectrophotometer with quartz cells and deionized water as a blank.

TEM analyses were performed using the JEOL JEM-2010F FasTem atomic resolution analytical microscope equipped with a field emission gun, with a resolution of 82 pm in STEM mode which allowed observing the atomic structure of the synthesized nanoparticles.

The antimicrobial activity of silver and titanium NPs obtained from peppermint and chamomile was evaluated. Model microorganisms were used for the study: *Escherichia coli* (Gram negative bacteria), which are microorganisms widely used in bacterial activity experiments and are associated with contamination by fecal matter in water, as well as the microorganism *Staphylococcus aureus* (Gram positive bacteria), this was done through the test of successive dilutions comparing the samples in dilutions that allow counting the number of CFU.

Results

The UV-Vis spectrum of the metallic nanoparticle samples was obtained to identify the maximum point of optical absorption, whose wavelength is associated with the excitation of the localized surface resonance plasmon and whose range is characteristic of nanomaterials, for the case of titanium nanoparticles with mint and chamomile a maximum absorption point was observed at 340 nm and 321 nm, respectively, and for the case of silver with mint and chamomile of 350 nm and 313 nm.

FTIR characterization allowed the identification of functional groups present in the phytomolecules existing in the mint and chamomile biomass extracts; bands at 3500 cm^{-1}, 2900 cm^{-1}, 1050 and 1150 cm^{-1} were identified, indicating the presence of O-H group stress vibrations, -CH stress vibrations and C-O stress vibrations, respectively, present in phytomolecules such as polyphenols.

The nanoparticles were characterized by transmission electron microscopy, the silver-mint nanoparticles obtained 26 nm in diameter, hexagonal crystal structure, crystallographic card 72-2108. The silver-chamomile nanoparticles a diameter of 6 nm, hexagonal crystal structure and crystallographic card 19-1155, both with a phase composition of Ag_2O.

The titanium nanoparticles of the titanium-mint system obtained nanoparticles with a diameter of 68 nm, orthorhombic crystalline structure and crystallographic card 16-0617. Finally, the titanium-chamomile system obtained the largest nanoparticles, diameter of 160 nm, tetragonal crystalline structure and crystallographic card 71-0650 both with TiO_2 phase composition.

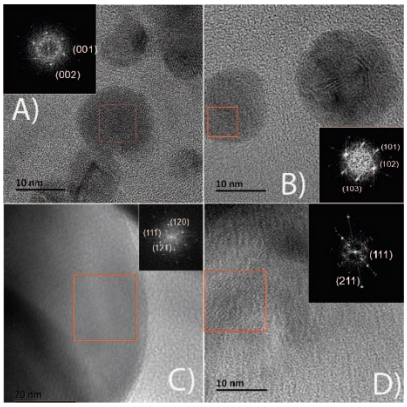

Figure 1.TEM images from A) MintAgNPs, B)ChamomileAgNps, C) MintTiNPs, B)ChamomileTiNps.

Microbiological tests were performed with the serial dilution method to identify the bactericidal capacity of the nanoparticles, using the model pathogenic bacteria, *Escherichia coli* and *Staphylococcus aureus*, Gram negative and Gram positive bacteria, respectively; in addition, the decrease in percentage of colony forming units (CFU) with respect to a sample without nanoparticle treatment was quantified. In this sense, and to determine the influence of each plant on the formation of nanoparticles, the concentration of total phenolic compounds was determined using the Folin-Ciocalteu reagent (Singleton, 1974), which was higher in chamomile (56.15) than in mint (50.45 mg/L), a result that was observed as a greater bactericidal capacity with respect to phytosynthesis with mint leaves.

Finally, it is important to highlight that the synthesis of metallic silver nanoparticles using mint and chamomile biomass is a viable synthesis method that allows obtaining metallic silver nanoparticles with high bactericidal capacity (>90%), against Gram-positive bacteria such as Staphylococcus aureus, and acceptable results against Gram-negative bacteria such as Escherichia coli (>80%); for the case of titanium nanoparticles the percentage of CFU reduction in bactericidal assays was lower (>70%).

Conclusions

The synthesis of metallic silver and titanium nanoparticles has proven to be an environmentally friendly methodology that is easy to perform and does not generate hazardous waste. Mint and Chamomile allowed obtaining Ag and Ti nanoparticles. With the FTIR technique, the presence of an organic fraction associated with the employed plant extract and the obtained metal nanoparticles was verified. The micrographs obtained by TEM, allowed to identify the structure of the synthesized systems, as well as the average diameter

The antibacterial capacity of the nanoparticles allows obtaining metallic silver nanoparticles with high bactericidal capacity (>90%), against Gram-positive bacteria such as *Staphylococcus aureus*, and acceptable results against Gram-negative bacteria such as *Escherichia coli* (>80%).

Acknowledgements

Salomón Mondragón is grateful to the CONACyT for scholarship (CVU 1137523), and to the Tecnológico Nacional de México (TeCNM)/ Instituto Tecnológico de Toluca for the support

References

[1]Huang, X., El-Sayed, M.A., 2010. Gold nanoparticles: optical properties and implementations in cancer diagnosis and photothermal therapy. J. Adv. Res. 1, 13–28. DOI:10.1016/j.jare.2010.02.002.
[2]Fahmy, S. A., Preis, E., Bakowsky, U., & Azzazy, H. M. E. S. (2020). Platinum nanoparticles: Green synthesis and biomedical applications. Molecules, 25(21), 4981. DOI:10.3390/molecules25214981
Rauwel, P., Küünal, S., Ferdov, S., & Rauwel, E. (2015). A review on the green synthesis of silver nanoparticles and their morphologies studied via TEM. Advances in Materials Science and Engineering, 2015. DOI: 10.1155/2015/682749
[3]Sadeghi, B., & Gholamhoseinpoor, F. (2015). A study on the stability and green synthesis of silver nanoparticles using Ziziphora tenuior (Zt) extract at room temperature. Spectrochimica Acta Part A: Molecular and Biomolecular Spectroscopy, 134, 310-315. DOI: 10.1016/j.saa.2014.06.046
[4] Velázquez-Hernández, M., Schabes-Retchkiman, P., Illescas, J., Macedo, M. G., González-Juárez, J. C., & Martínez-Gallegos, S. (2019). Ag, Zn and Cu nanoparticles synthesized from Eichhornia crassipes leaf extracts and their application in phenol photocatalytic degradation. MRS Advances, 4(59-60), 3251- 3258

POLYBENZIMIDAZOLES FOR GAS SEPARATION: SYNTHESIS AND MODIFICATION

Jessica Olvera-Mancilla, Mario Rojas-Rodríguez, Miriam Garcia-Vargas, Lioudmila Fomina, Carla Aguilar-Lugo and Larissa Alexandrova

Instituto de Investigaciones en Materiales, Universidad Nacional Autónoma de México, Circuito Exterior s/n, Ciudad Universitaria, 04510, México D.F.; México

Introduction.

Aromatic polybenzimidazoles (PBIs) have excellent thermo-mechanical properties and high chemical stability [1], that together with their high intrinsic H_2/CO_2 selectivity makes PBIs desired candidates for gas separation in harsh environments [2]. However, such applications are restricted due to their low gas permeabilities. Furthermore, the vast majority of PBIs produced by the traditional methods have very poor solubility in organic solvents. Several strategies have been employed to overcome these drawbacks, such as ether bridges, thermal rearrangement of soluble precursors, and N-substituted modifications of already synthesized polymers [3]. All these enhanced gas permeability but the improvements were not very impressive, particularly in comparison with the synthetic efforts made.

Recently a new family of membrane materials obtained by the controlled pyrolysis of the polymeric precursors, so called carbon molecular sieve membranes (CMSMs), has been developed [4,5]. In contrast to the conventional polymeric membranes exhibiting an intrinsic trade-off between permeability and selectivity (Robeson's upper bound) [6], CMSMs demonstrate both high permeability and selectivity for challenging gas separations, such as N_2/CH_4, CO_2/CH_4 and olefin/paraffin overpassing the upper-bound limit [7]. Additionally, CMSMs show excellent thermo-chemical stability and resistance to plasticization. Thus, CMSMs are promising candidates for membranes operating under high temperature and aggressive conditions.

The choice of polymeric precursors for the formation of CMSMs is very important: the precursors should be thermally stable and of high molecular weight to sustain the pyrolysis high temperature and wouldn’t convert into extremely brittle materials. Aromatic polyimides have been the most studied precursors because they are easy to produce with high molecular weights and have good thermo-chemical stability [6], but only a few studies have been published on PBI-based CMSMs [8-10].

Recently, our group reported fast method for formation of high molecular weight and soluble PBI (PBI-6F) based on bulky (hexafluoroisopropylidene)bis(benzoic acid) (HFA) (see Scheme 1) [11]. In view of such PBI-6F features, we considered it as an interesting candidate for the preparation of CMS membrane. The characterization and properties of this CMSM are reported and discussed.

Experimental.

PBI-6F was synthesized by solution polycondensation in Eaton reagent (ER) using equimolar amounts of 3,3’-diaminobenzidine (DAB) and HFA [11].

The membrane was prepared by casting from a previously filtered polymeric solution in DMF at room temperature. The details are reported in [12].

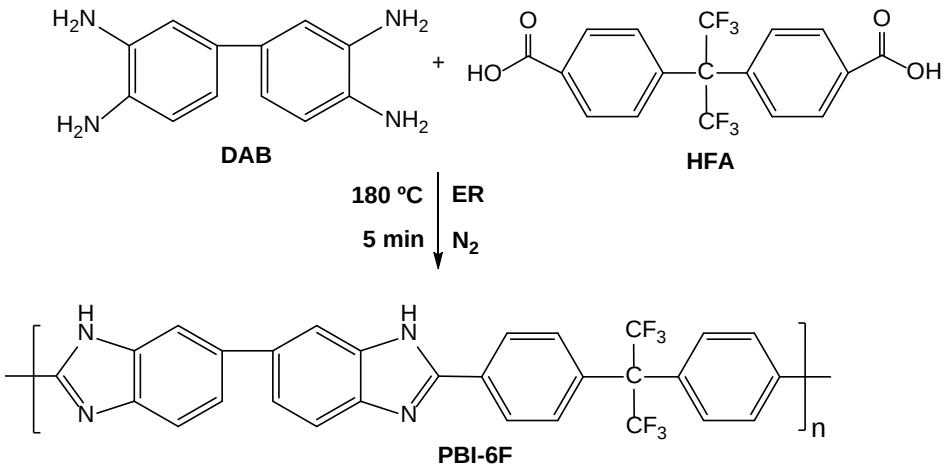

Scheme 1. Synthesis of PBI-6F.

CMSM-600 was obtained by pyrolysis of PBI-6F film in Ar using a stepwise temperature regime with final temperature of 600 ºC [X]

Results and Discussion

The material obtained after pyrolysis may be described as a self-supported dark brown, almost black, film, which was more fragile than the precursor, but it was manageable enough to run all the measurements. The membrane was named CMSM-600 and characterized by FT-IR, Raman and XPS spectroscopies, elemental analysis and wide-angle X-ray diffraction (WAXD) to disclose its possible structure [11].

The comparison of FT-IR spectra of PBI-6F and CMSM-600 showed that all PBI-6Fcharacteristic bands, such as a broad absorption in 3500-2800 cm^{-1} (from n N–H), bands at 1620 cm^{-1} and 1550–1400 cm^{-1} due to C=N and C=C vibrations; and between 1260 and 1115 cm^{-1} due to n C–F, disappeared after the pyrolysis; only two medium intensity bands at 1650 and 1540 cm^{-1} were seen in the spectrum of CMSM-600. These bands correspond to the highly sp^2 hybridized systems originated from C=C and C=N bonds.

TGA analysis displayed a dramatic weight loss from 500 °C to 580 °C associated with carbonization, where the conjugated carbon-carbon and carbon-nitrogen systems formed along with the elimination of CF_3 moieties. The last process could be particularly important for permeability improvement in CMSMs because it may produce more open micropores due to bulkiness of CF_3.

The WAXD analysis also revealed an important difference in the precursor and CMCM-600 structures. Both exhibited halo characteristic for amorphous materials, but X-ray pattern of CMCM-600 showed feature of graphite like structure with presence of micropores observed at very small 2θ angle in the diffractogram.

The Raman and XPS spectroscopies additionally confirmed porous pseudo graphitic type (turbostratic) structure of CMSM-600, consisting of strands formed by aromatic sp^2 hybridized carbons. The strands align in form of plates producing ultra-micropores and the plates are further arranged in tighter constructions, where the space between parallel plates forms the micropores.

The pyrolysis of PBI-6F gives rise to the formation of these aromatic strands by two principal processes: decomposition of the imidazole rings and defluorination. The CMSM-600 strands are proposed to be composed by a mixture of pyrazine and pyrrole type structures which are shown in Figure 1.

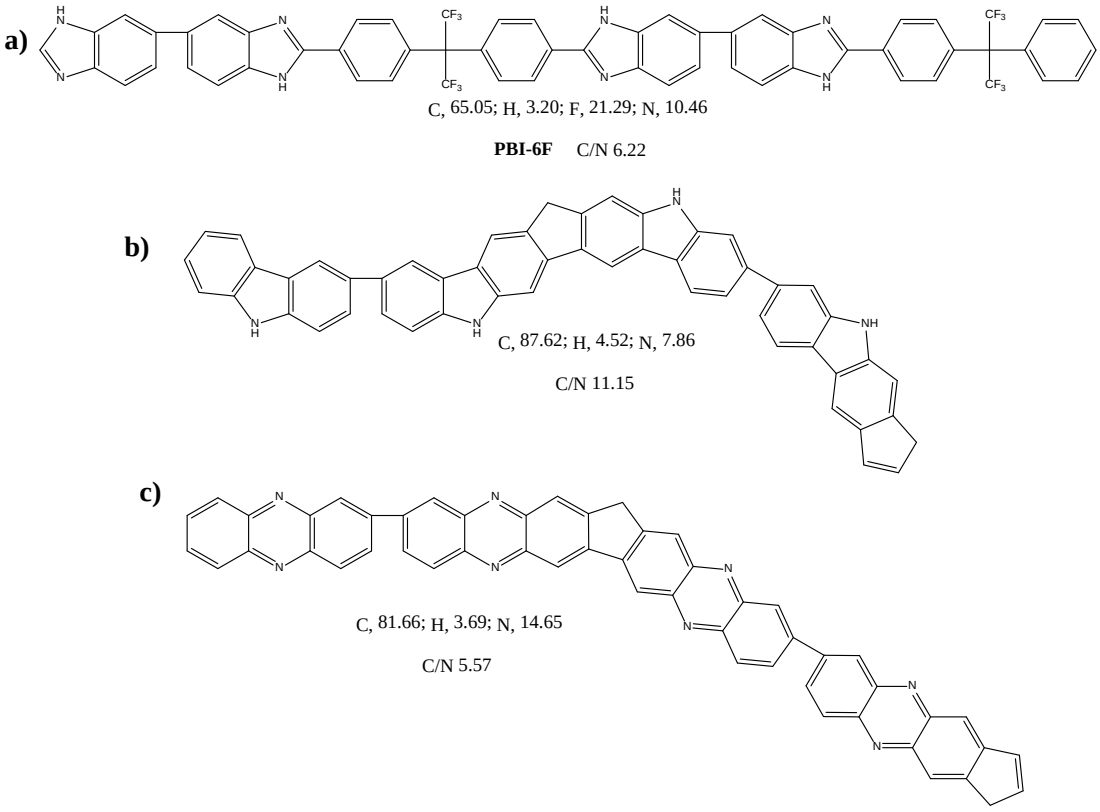

Figure 1. Possible structures after pyrolysis of PBI-6F and their C/N relationship: a) Precursor PBI-6F, b) Pyrrole-type strand and c) Pyrazine-type strand.

The CMSM-600 and its precursor, PBI-6F, gas separation performances for CO_2/N_2, O_2/N_2, CO_2/CH_4 and H_2/CO_2 pairs are shown in a Robeson plot in Figure 2 in comparison with other pyrolyzed CMSMs obtained from PBI precursors. As can be seen CMSM-600 membrane shows an extraordinary improvement in permselectivity for all gas pairs tested, surpassing 2008 Robeson limit. The other PBI-based carbonized membranes reported did not demonstrate such good permselectivity, except PBI-800 and PBI-900 (Fig. 2d). But even the last two membranes were good for H_2/CO_2 separation only, and not for other gas pairs. It is important to note that fluorinated structures were not used in none of the reported PBI precursors. Thus, we believe that the presence of bulky $–C(CF_3)-$ substituent in the precursor is a crucial factor to form during pyrolysis a less dense highly permeable membrane.

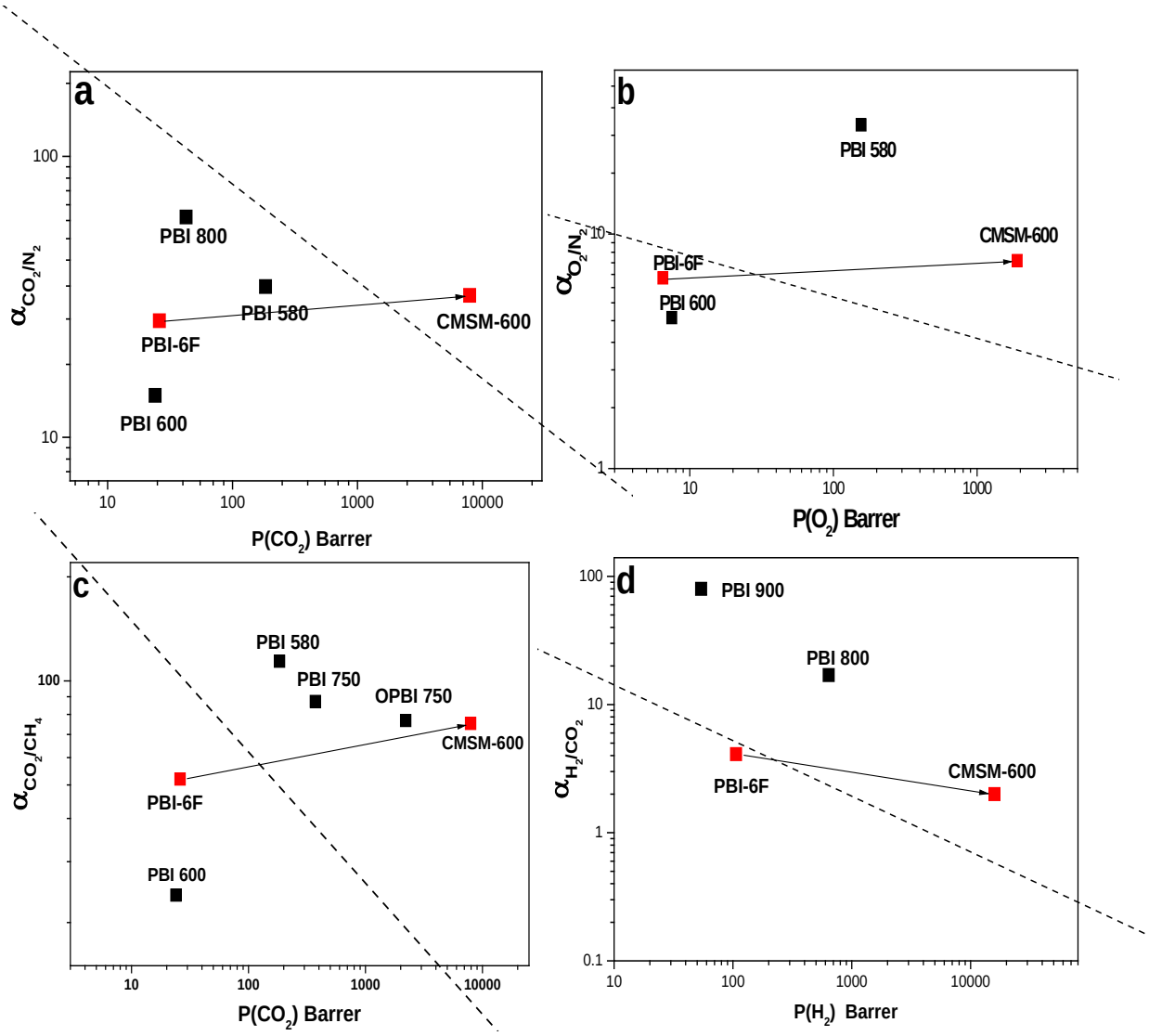

Figure 2. Separation performance for PBI-6F and CMSM-600 for a) CO_2/N_2, b) O_2/N_2, c) CO_2/CH_4 and d) H_2/CO_2 in comparison with other PBI-based CMSMs [5, 8-10]. 2008 Robeson upper plot is shown as dash line.

Acknowledgement

This work was financially supported by PAPIIT AG100323 and CONAHCyT CF-2023-G-220 projects. The authors thank technician staff of IIM-UNAM for the analyses: M.A. Canseco Martinez, G. Cedillo Valverde, S. Lopez Morales, E. Hernandez Mecinas, A. Tejeda Cruz, E. Reyes Morales.

References

1. Buckley A., Stuetz D.E., Serad G.A. *Encyclopedia of Polymer Science and Engineering.*; J. Wiley & Sons: New York, **1986**

2. Borjigin H., Stevens K.A., Liu R., Moon J.D., Shaver A.T., Swinnea S., Freeman B.D., Riffle J.S., McGrath J.E. *Polymer (Guildf).* **2015**, *71*, 135–142.

3. (a) Olvera-Mancilla J., Aguilar-Lugo C., Fernández-Gijón C.A., Palacios-Alquisira J., Zolotukhin M., Alexandrova L. *ChemistrySelect* **2020**, *5*(17), 5082–5091; (b) Kumbharkar S.C., Karadkar P.B., Kharul U.K. *J. Memb. Sci.* **2006**, *286* (1–2), 161–169

4. Saufi S., Ismail A. *Carbon N. Y.* **2004**, *42* (2), 241–259

5. Adams J.S., Itta, A.K., Zhang C., Wenz G.B., Sanyal O., Koros W. J. *Carbon N. Y.* **2019**, *141*, 238–246

6. Robeson L.M. *J. Memb. Sci.* **2008**, *320* (1–2), 390–400.

7. Kim S.-J., Kwon Y., Kim D., Park H., Cho Y.H., Nam, S.-E., Park, Y.-I. *Membranes (Basel)* **2021**, *11*(7), 482.

8. Jiao W., Ban Y., Shi Z., Jiang X., Li Y., Yang W. *J. Memb. Sci.* **2017**, *533*, 1–10;

9. Pérez-Francisco J.M., Santiago-García J.L., Loría-Bastarrachea M.I., Paul D.R., Freeman B.D., Aguilar-Vega M. *J. Memb. Sci.* **2020**, *597*, 117703

10. Omidvar M., Nguyen H., Liang H., Doherty C.M., Hill A.J., Stafford C.M., Feng X., Swihart M.T., Lin H. *ACS Appl. Mater. Interfaces* **2019**, *11*(50), 47365–47372.

11. Olvera-Mancilla J., Palacios-Alquisira J., Alexandrova L. *High Perform. Polym.* **2018**, *30*(6), 699–709

12. Olvera-Mancilla J., Aguilar-Lugo C., Fomina L., Sanchez-Arevalo F.M., Gonzalez-Diaz M.O., Sulub-Sulub R., Aguilar-Vega M., Alexandrova L. *Ind. Eng. Chem. Res.* **2022**, *61*, 6587-6599.

Polymat Contributions

Synthesis and characterization of polynorbornene dicarboximides bearing thiol groups for heavy metal adsorption from aqueous media

Alejandro Onchi[1], Carlos Corona-García[1], Arlette A. Santiago[2], Mercedes Gabriela Téllez Arias[3], Joel Vargas[1*]

*[1]Instituto de Investigaciones en Materiales, Unidad Morelia, Universidad Nacional Autónoma de México, Antigua Carretera a Pátzcuaro No. 8701, Col. Ex Hacienda de San José de la Huerta, C.P. 58190, Morelia, Michoacán, México. *jvargas@iim.unam.mx*
[2]Escuela Nacional de Estudios Superiores, Unidad Morelia, Universidad Nacional Autónoma de México, Antigua Carretera a Pátzcuaro No. 8701, Col. Ex Hacienda de San José de la Huerta, C.P. 58190, Morelia, Michoacán, México.
[3]Universidad Michoacana de San Nicolás de Hidalgo, Facultad de Ingeniería Química, México.

The contamination of water resources with heavy metals is a very serious concern that demands prompt and effective attention due to the serious health risks caused by these contaminants. The synthesis and ring-opening metathesis polymerization (ROMP) of novel norbornene dicarboximides bearing thiol pendant groups, specifically, *N*-4-thiophenyl-*exo*-norbornene-5,6-dicarboximide (**1a**), *N*-4-(methylthio)phenyl-*exo*-norbornene-5,6-dicarboximide (**1b**) and *N*-4-(trifluoromethylthio)phenyl-*exo*-norbornene-5,6-dicarboximide (**1c**), to render them adsorbents for the removal of heavy metal ions from water is reported in this study. The polymers were characterized by NMR, TGA and, subsequently, an isothermal study of the adsorption in aqueous solutions of Pb^{2+}, Cd^{2+} and Ni^{2+} was carried out to study the capacity of heavy metal adsorption in each polymer. The maximum removal amounts were found to be 53.7 mg/g for Pb^{2+}, 43.8 mg/g for Cd^{2+} and 29.1 mg/g for Ni^{2+} in the SH-bearing polymer **2a**, 46.4 mg/g for Pb^{2+}, 32.9 mg/g for Cd^{2+} and 27.1 mg/g for Ni^{2+} in the SCH_3-bearing polymer **2b**, and 40.3 mg/g for Pb^{2+}, 35.9 mg/g for Cd^{2+} and 27.8 mg/g for Ni^{2+} in the SCF_3-bearing polymer **2c**, respectively. The higher heavy metal removal capacity of polymer **2a** was attributed to the lower steric hindrance and higher hydrophilicity imparted by −SH groups to the polymer. The results show that these novel thiol-functionalized polymer-based adsorbents are effective for the removal of heavy metal ions from water.

Introduction

In recent years there has been a concerning increase in the amount of heavy metals found in affluents, due to the steady rise of the industrial activities [1,2]. There are several techniques that are known to be effective in the elimination of heavy metals in aqueous media, such as osmosis, ion exchange, chemical precipitation and adsorption, among others [3–5]. Adsorption is a very interesting method due to its versatility, high efficiency and the large number of adsorbents available [6,7]. Polymers are chemically stable in water and norbornene-based monomers can be easily polymerized using the ring-opening metathesis polymerization (ROMP) technique. These monomers can be functionalized for heavy metal adsorption making the preparation of systematic series of norbornene derivatives an attainable goal [8–10].
Among the many functional group options used to endow materials with adsorption properties, thiols have drawn much attention and are well known for their ability to coordinate with divalent ions such as Pb^{2+}, Cd^{2+} and Ni^{2+} [11,12].

Thus, in this study, we have undertaken the synthesis and ROMP of three new norbornene dicarboximide monomers bearing thiol pendant groups along with the assessment of these novel polymers as adsorbents for the removal of Pb^{2+}, Cd^{2+} and Ni^{2+} from water.

Methodology

30 mL of dichloromethane were used to dissolve 0.1 mol of NDA and 0.1 mol of 4-aminothiophenol, 4-(methylthio)aniline, 4-(trifluoromethylthio)aniline to synthesize monomers **1a**, **1b** and **1c**, respectively. The solutions were heated at 60 °C and kept with constant stirring for 12 h to give their respective amic acid. The amic acids obtained were dissolved in 30 mL of acetic anhydride, then 0.5 g of anhydrous sodium acetate were added to each solution and kept with constant stirring at 70 °C for 12 h. The reaction mixtures were poured into iced water and the solids obtained were filtered. Finally, the monomers were recrystallized twice from a toluene:hexane (1:1) solution, ethanol and hexane, respetively. The final products were obtained in 72%, 61% and 49% yield, respectively. The melting point (MP) of each monomer was found to be: **1a**) 166-168 °C, **1b**) 164-166 °C and **1c**) 157-159 °C.
Once obtained the purified monomers, the polymerization reactions were carried out in glass vials under nitrogen atmosphere using the second generation Grubbs catalyst in 1,2-dichloroethane to obtain polymers **2a**, **2b** and **2c**, respectively. Ethyl vinyl ether was employed as inhibitor in the final stage and the polymers were obtained by pouring the reaction solution into 50 mL of hot stirring methanol, containing three drops of 1 N HCl, precipitating in the form of white fibers. The resulting polymers were collected by filtration, then dissolved in chloroform and poured again into hot stirring methanol for being purified. Finally, the polymers were dried under vacuum at 40 °C overnight (**Figure 1**).

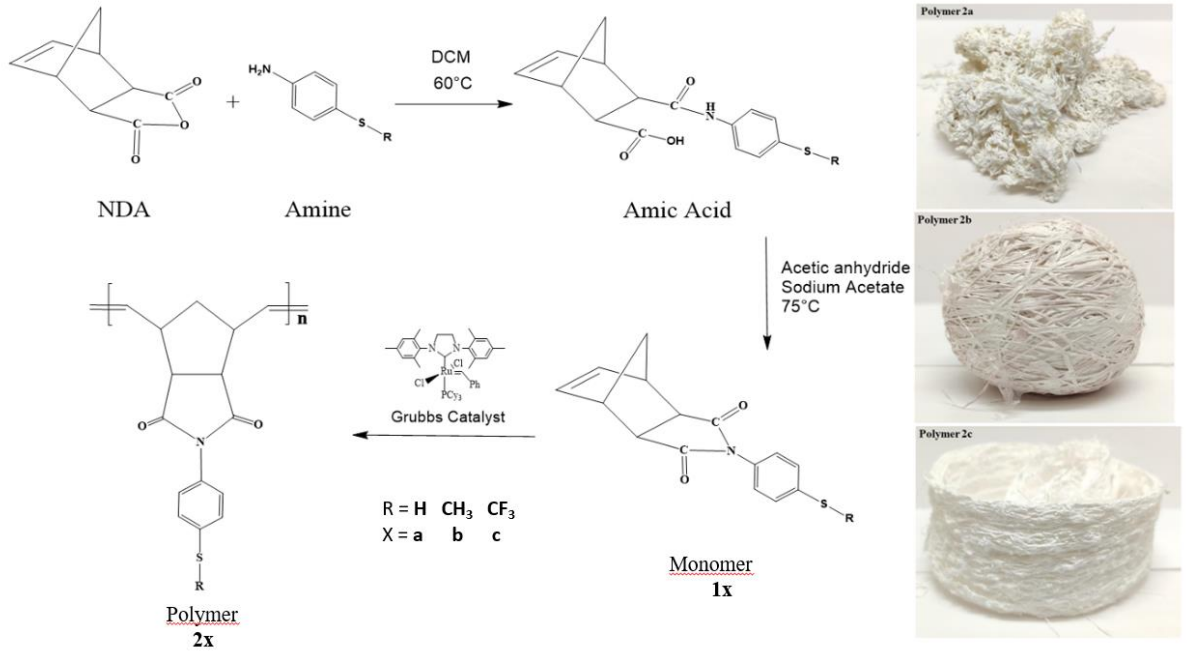

Figure 1. Synthesis route of polymers **2a**, **2b** and **2c** with their respective photographic images.

Results

Pb^{2+}, Cd^{2+} and Ni^{2+} stock solutions of 1000 mg/L were prepared by dissolving $PbCl_2$, $CdCl_2 \cdot 2.5H_2O$ and $NiCl_2 \cdot 6H_2O$, respectively, in deionized water. Before each series of atomic absorption spectroscopy (**AAS**) measurements, the deionized water, used in the adsorption experiments, was used as a blank to discard any heavy metal trace that could be in the remaining liquid. Subsequently, each heavy metal solution concentration was corroborated using AAS before the respective experiments.

Pb^{2+}, Cd^{2+} and Ni^{2+} solutions were prepared at different concentrations (10, 20, 40, 60, 80, 100, 200, 300, 400 and 500 ppm) and 0.01 g of each polymer was added to every solution separately and was kept with constant stirring in a rotatory shaker for 24 h. After the contact time, the samples were centrifuged for 10 min at 3500 rpm to separate the polymer from the solution. The final heavy metal concentration of the solutions in the remaining liquid was determined using AAS.

The maximum equilibrium adsorption capacity (q_e) of the three polymers as a function of the heavy metal solution concentration (C_e) can be observed in **Figure 2**. The results show that the q_e increases while C_e also increases, where Pb^{2+} has the largest variation of the three divalent ions. The q_e for polymer **2a** was found to be 53.78 mg/g for Pb^{2+}, 43.80 mg/g for Cd^{2+} and 29.10 mg/g for Ni^{2+}. The q_e for polymer **2b** was found to be 46.45 mg/g for Pb^{2+}, 32.95 mg/g for Cd^{2+} and 27.10 mg/g for Ni^{2+}. The q_e for polymer **2c** was found to be 40.31 mg/g for Pb^{2+}, 35.93 mg/g for Cd^{2+} and 27.84 mg/g for Ni^{2+}. The higher heavy metal adsorption capacity of polymer **2a** could be ascribed to the lower steric hindrance imparted by –SH groups to the polymer backbone compared to those of $–SCH_3$ and $–SCF_3$ groups in polymers **2b** and **2c**, respectively. The aforementioned, in conjunction with the higher hydrophilic character of the –SH groups could favor the water absorption by the polymer matrix, thus promoting the coordination between the polymer and the heavy metals during the ion adsorption process.

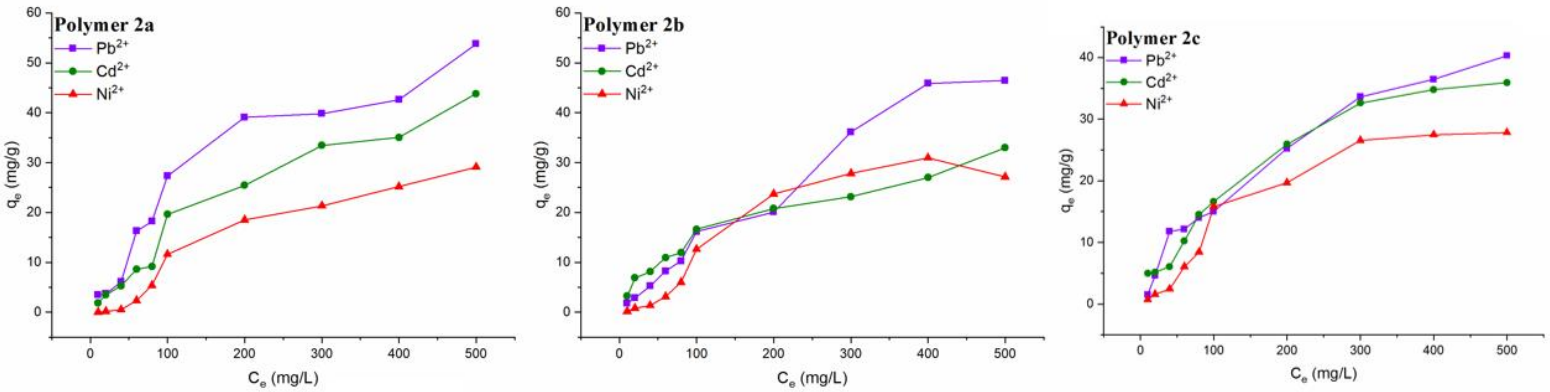

Figure 2. Adsorption capacity of Pb^{2+}, Cd^{2+} and Ni^{2+} of the polymers **2a**, **2b** and **2c**.

Conclusions

Novel thiol-functionalized polynorbornene dicarboximides were successfully synthesized by ring-opening metathesis polymerization (ROMP) and fully characterized by FT-IR and NMR. The adsorptions of Pb^{2+}, Cd^{2+} and Ni^{2+} ions in the polymers **2a**, **2b** and **2c** were investigated

by batch adsorption experiments revealing that the affinity and the maximum removal capacity in the thiol-functionalized polymers decreased in the order Pb^{2+} > Cd^{2+} > Ni^{2+}. The adsorption capacity is attributed to the coordination that occurs between the sulfur atom of the thiol groups and the divalent ions. The higher heavy metal removal capacity of polymer **2a** was attributed to the lower steric hindrance and higher hydrophilicity imparted by −SH groups to the polymer backbone compared to those of $-SCH_3$ and $-SCF_3$ groups in polymers **2b** and **2c**, respectively. According to the outcomes, polynorbornene dicarboximides containing thiol groups could potentially be used in the cleanse of contaminated water due to their effectiveness as heavy metal adsorbents.

Acknowledgements

Financial support from DGAPA-UNAM PAPIIT through the project IN108022 is gratefully acknowledged. We are grateful to Gerardo Cedillo Valverde for his assistance in NMR characterization.

References

1. Jabeen, A.; Huang, X.; Aamir, M. The Challenges of Water Pollution, Threat to Public Health, Flaws of Water Laws and Policies in Pakistan. *J Water Resour Prot* **2015**, *07*, 1516–1526, doi:10.4236/jwarp.2015.717125.
2. World Health Organization *Guidelines for Drinking-Water Quality*; Fourth Edition.; 2017;
3. Ghosh, P.; Samanta, A.N.; Ray, S. Reduction of COD and Removal of Zn2+ from Rayon Industry Wastewater by Combined Electro-Fenton Treatment and Chemical Precipitation. *Desalination* **2011**, *266*, 213–217, doi:10.1016/j.desal.2010.08.029.
4. Huang, J.-H.; Zeng, G.-M.; Zhou, C.-F.; Li, X.; Shi, L.-J.; He, S.-B. Adsorption of Surfactant Micelles and Cd2+/Zn2+ in Micellar-Enhanced Ultrafiltration. *J Hazard Mater* **2010**, *183*, 287–293, doi:10.1016/j.jhazmat.2010.07.022.
5. Pruvot, C.; Douay, F.; Hervé, F.; Waterlot, C. Heavy Metals in Soil, Crops and Grass as a Source of Human Exposure in the Former Mining Areas (6 Pp). *J Soils Sediments* **2006**, *6*, 215–220, doi:10.1065/jss2006.10.186.
6. Ipek, U. Removal of Ni(II) and Zn(II) from an Aqueous Solutionby Reverse Osmosis. *Desalination* **2005**, *174*, 161–169, doi:10.1016/j.desal.2004.09.009.
7. Razzak, S.A.; Faruque, M.O.; Alsheikh, Z.; Alsheikhmohamad, L.; Alkuroud, D.; Alfayez, A.; Hossain, S.M.Z.; Hossain, M.M. A Comprehensive Review on Conventional and Biological-Driven Heavy Metals Removal from Industrial Wastewater. *Environmental Advances* **2022**, *7*, 100168, doi:10.1016/j.envadv.2022.100168.
8. Cruz-Morales, J.A.; Vargas, J.; Santiago, A.A.; Vásquez-García, S.R.; Tlenkopatchev, M.A.; de Lys, T.; López-González, M. Synthesis and Gas Transport Properties of New Polynorbornene Dicarboximides Bearing Trifluoromethyl Isomer Moieties. *High Perform Polym* **2016**, *28*, 1246–1262, doi:10.1177/0954008315624954.
9. Ruiz, I.; Corona-García, C.; Santiago, A.A.; Abatal, M.; Téllez Arias, M.G.; Alfonso, I.; Vargas, J. Synthesis, Characterization, and Assessment of Novel Sulfonated Polynorbornene Dicarboximides as Adsorbents for the Removal of Heavy Metals from Water. *Environmental Science and Pollution Research* **2021**, *28*, 52014–52031, doi:10.1007/s11356-021-13757-1.
10. Maya, V.G.; Contreras, A.P.; Canseco, M.-A.; Tlenkopatchev, M.A. Synthesis and Chromium Complexation Properties of a Ionic Polynorbornene. *React Funct Polym* **2001**, *49*, 145–150, doi:10.1016/S1381-5148(01)00073-6.
11. Xia, Z.; Baird, L.; Zimmerman, N.; Yeager, M. Heavy Metal Ion Removal by Thiol Functionalized Aluminum Oxide Hydroxide Nanowhiskers. *Appl Surf Sci* **2017**, *416*, 565–573, doi:10.1016/j.apsusc.2017.04.095.
12. Zhang, W.; Cai, Y.; Downum, K.R.; Ma, L.Q. Thiol Synthesis and Arsenic Hyperaccumulation in Pteris Vittata (Chinese Brake Fern). *Environmental Pollution* **2004**, *131*, 337–345, doi:10.1016/j.envpol.2004.03.010.

Session 5.- Materials Science Applied to Industry

CIRCULAR BIOECONOMY OPPORTUNITIES IN NEW MATERIALS: THE CASE OF MORELOS´ RICE IN MEXICO.

América A. Padilla Viveros[1]

[1]Science, Technology and Society Program, Center for Research and Advanced Studies, Mexico City, 07360. aviveros@cinvestav.mx

Keywords: circular bioeconomy, appellations of origin, rice, Mexico.

INTRODUCTION

The circular bioeconomy focuses on biomass's sustainable, resource-efficient valorization in integrated, multi-output production chains while using residues and wastes and optimizing biomass value over time via cascading. Such optimization can focus on economic, environmental, or social aspects and ideally considers all three pillars of sustainability (Stegmann et al. 2020). The circular bioeconomy model has had successful results in the Latin American countries where it has been used. Still, efforts are needed to promote public policies and take advantage of good practices and lessons to trigger its use (IICA et al. 2019). There is a long way in the region to build policy strategies for development and have adequate regulatory frameworks that allow the progress of new markets and value chains, integrating rural development and sustainable production. The appellation of origin (AO) is a particular type of geographical indication that consists of a geographical name, or a traditional designation used for products with specific qualities or characteristics that can be attributed mainly to the geographical environment of production (WIPO, 2022). Well-applied AO can support local or regional rural development, notoriety, collective action of producers, the reappropriation of biocultural heritage, and the coordination of actors in the production value chain. However, their impact is not always positive since they can become a factor of exclusion for peasant producers of raw materials. They may not consider the working conditions of wage earners. There is no guarantee that the territorial income will be distributed downstream and upstream in the food value chain (Andrés-Rosales et al., 2018; Renard and Domínguez-Arista, 2019). The benefits for the local producer depend on the institutional structure for the recognition and fostering of the AO. The system, in turn, is a consequence of the power relations that govern its construction. In Mexico, the AO tends to reinforce the industrial elites and the exclusion of peasants. The added value generated by the AO does not reach the hands of the farmers. Although they are linked to a particular territory, AO products are directed at national and international markets, where there is occasionally tremendous pressure to increase production and respond to demand encouraged by the reputation of the products. This demand causes overexploitation of natural resources and leads to the search for ingredients outside the territory of origin, violating the AO directions. Although the standards are quality guarantees, they lead to a homogenization of production and the establishment of

monocultures instead of artisanal products. In addition, some AO cover too large regions without recognizing geographic diversity. When granting AO in Mexico, power relations and the logic of commercial protection weigh more than a search for inclusive territorial development (Diego-Fernandez 2021).

Rice of Morelos State

The state of Morelos, Mexico, is traditionally a rice-growing state, recognized for the quality of its products nationally and internationally because it has preserved, since its origin, unique and exclusive agronomic, milling, and culinary characteristics. The state's area cultivated under rice has decreased in the last 15 years because of competition from imported rice (Ireta-Paredes et al. 2015). The rice that is produced in the state of Morelos is the result, not only of the fortune of the characteristics of the soil and climate but also of a series of conjuncture, endogenous and organizational processes between the rice farmers and the various local institutions involved through the years (Tolentino 2013).

In this context, the aim of this research is to perform a scouting of circular bioeconomy opportunities in the rice from the State of Morelos, a product with appellation of origin in Mexico for promoting rural development by applying sustainable principles.

METHODOLOGY

We conducted transdisciplinary research with a mixed approach (descriptive and semi-quantitative) to map the value chain of AO and perform a patent landscape in WIPO database to understand the value chains adjustments into the circular bioeconomy model to generate added value products to foster rural development.

FINDINGS

Processes and by-products in rice production

The certification and recognition mechanisms that allow the producer to be present in global markets and the market niches of developed countries have been put in check; although they have contributed to the constitution and reproduction under the approach of Localized Agri-Food Systems (SIAL), it has resulted in self-exploitation and self-exclusion (Torres, 2012; Tolentino 2013). There is, therefore, the presence of a paradox where consumers are increasingly attracted to products with specific characteristics associated with a territory or intrinsic value in combination with the social exclusion that gives rise to new inequalities and asymmetries in the organization and collective action (Torres and Muchnik, 2012). This position alludes to recognizing ethical and political dimensions and seeks an institutional perspective for constructing alternatives to combat poverty (Tolentino, 2013). Most of the rice farmers of the area can't compete with imported rice and helped to identify the alternative strategy of differentiating production (Ireta-Paredes et al. 2015) even though it grants the AO recognition. Processes and by-products in rice production are presented in Figure 1.

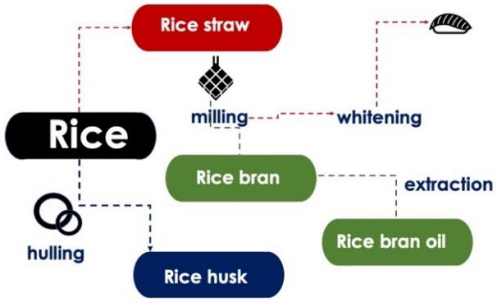

Figure 1 Processes and by-products in rice production. Adapted from Le et al. 2022.

Opportunities offered by circular bioeconomy through the AO on Morelos State Rice.

Improving biomass utilization productivity following cascading strategy is a priority for the biorefinery-based circular bioeconomy. In recent years, energy research has seen an increasing interest in bio-products from paddy-based biorefinery, but the utilization of the entire value of paddy biomass to guide the commercial viability of its products has not been got feasible outcomes. A potential pathway for a conceptual paddy biorefinery framework by addressing wastes for producing more products has been proposed. The waste conversion demonstrated the integrated biorefinery's feasibility in value-added products such as nano-silica and lignin. Silica recovered from the bioethanol system was continued to be reused to produce ZSM-5 and Ni/ZSM-5 as catalysts of rice straw lignin depolymerization, achieving a high conversion of lignin up to 95% and fair yield of the phenolic products up to 41% (figure 2a). The material flow of an integrated biorefinery model was reported to give an outlook for making most of the processing routes of rice residues, establishing a life cycle that follows the circular bioeconomy concept, and the relationship between each potential bioproducts and their market opportunities (Le et al. 2022).

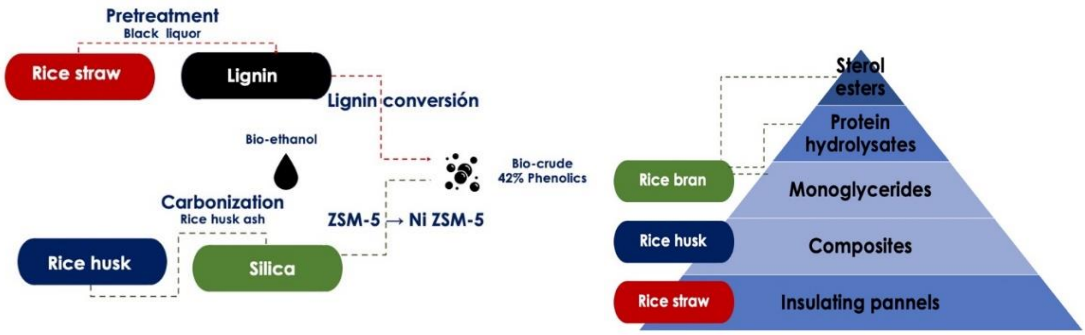

Figure 2 a) Improvement of rice biomass utilization productivity following cascading for the biorefinery-based circular bioeconomy. Conversion of wastes into value-added products such as nano-silica and lignin. Silica recovered from bioethanol system was continued to be reused to produce ZSM-5 and Ni/ZSM-5 as catalysts of rice straw lignin depolymerization achieving high conversion of lignin up to 95% and fair yield of phenolic products up to 41%. b) Pyramid of added value bioproducts from byproducts of rice. Adapted from Le et al. 2022.

Rice husk (RH) is a natural sheath that forms around rice grains during their growth. RH can be used as filler in composite materials in various polymer matrices as a type of natural fiber obtained from agro-industrial waste (Le et al. 2022) (Figure 2b). The application of RH-filled composites as alternative materials in building and construction is possible, with both lightweight and low cost being their main driving forces (Reza et al. 2015). RH is a cellulose-based fibrous material with a wide range of aspect ratios (Chand et al., 2010). The principal components of RH are cellulose (25-35%), hemicellulose (18-21%), lignin (26-31%), and SiO_2 (silica) (15-17%) (Reza et al., 2015). Due to its high availability, low bulk density, toughness, abrasiveness in nature, resistance to weathering, and unique composition, a variety of applications have been proposed in the literature. RH has the potential to be utilized as an insulating material in the production of organic chemicals (Das et al. 2014), panel boards and activated carbon (Mishra et al. 1986), and supplementary bonding material (Aprianti et al. 2015). The potential of RH as a source of power generation and its financial liabilities have also been studied (Kapur et al.1996; Sookkumnerd et al. 2005). Even though some of this husk is converted into the mentioned end products, like many other agricultural byproducts, the industrial applications of this biomass are still limited, with little economic value. Therefore, sustainable pathways to reutilize the RH are fundamental. Research is currently undertaken worldwide to identify potential applications and develop economically feasible processes for these applications on a commercial scale (Reza et al., 2015). Small power plants have been using rice husks as biofuel for brick production, generating heat, and steam to power rice dryers and rice mills for a long time. In recent years, some manufacturers have purposed RH as the raw material for both biodegradable, and more eco-friendly plastic composite products, as foodstuff containers, food packaging, and tableware. Around 0.28 kg of rice husk is peeled off from each kilogram of milled white rice, allowing water-resistant manufacturing products and low thermal conductivity. Many companies have launched eco-friendly rice husks and food contact products, such as food containers, plates, bowls, lunch boxes, cups, forks, knives, and chopsticks. Some manufacturers claim that their products are 100% biodegradable or household-compostable because they are made with rice husks and not mixed with plastics to create a composite. This is possible because the cellulose and lignin in rice husks provide a sturdy texture to the products. However, a large part of the products that contain rice husk also contains resins and other chemicals to enhance the product performance, such as resistance, flexibility, and durability (figure 2a). In this case, the products are not biodegradable. An area of opportunity identified for rice from the state of Morelos is altogether avoiding the use of plastic on the packaging. Instead, it would replace composite materials from rice husks RH. Agricultural waste is a rich source of various nanomaterials, such as nano-silica (NS), nano-carbon (NC), and nano-zeolite (NZ) (Ali et al. 2021).

CONCLUSIONS

Rethinking an economy based on sustainable biocultural heritage management is fundamental in Mexico. Well-applied AO can support local or regional rural development, the reappropriation of biocultural heritage, and coordinating actors in the production value chain. However, their impact is not always positive since they can become a factor of exclusion for peasant producers of raw materials. Moreover, there is no guarantee that the territorial income will be distributed downstream and upstream in the food value chain. Our first approach evidenced the benefits and opportunities for applying the bioeconomy in the rice of Morelos state and promoting rural development.

REFERENCES

1. Ali S.H, Emran M.Y. and Gomaa H (2021) Rice Husk-Derived Nanomaterials for Potential Applications, Waste Recycling Technologies for Nanomaterials Manufacturing. Chapter 25. ISBN: 978-3-030-68030-5
2. Andrés-Rosales R, Bustamante LC and Ramírez AGS. (2018) Social Exclusion and Economic growth in the Mexican Regions: A Spatial Approach, Journal of Regional Research, no. 40, pp. 57-78.
3. Aprianti E., Shafigh, Bahri S. and Farahani J.N. (2015) Supplementary cementitious materials origin from agricultural wastes—a review *Construction and Building Materials*, vol. 74, pp. 176– 187.
4. Chand, P. Sharma, and Fahim M. (2010) Tribology of maleic anhydride modified rice-husk filled polyvinylchloride, *Wear*, vol. 269, no. 11-12, pp. 847–853, 2010.
5. Das A. M., Ali A. A., and Hazarika M. P. Synthesis and characterization of cellulose acetate from rice husk: eco-friendly condition, Carbohydrate Polymers, vol. 112, pp. 342–349, 2014.
6. Diego-Fernández M. (2021). En México, la Denominación de Origen suele reforzar a las élites industriales. Resonancias. Blog del Instituto de Investigaciones Sociales de la UNAM. https://www.iis.unam.mx/blog/en-mexico-la-denominacion-de-origen-suele-reforzar-a-las-elites-industriales/
7. IICA (Inter-American Institute for Cooperation on Agriculture, Costa Rica); FAO (Food and Agriculture Organization of the United Nations, Italy); ECLAC (Economic Commission for Latin America and the Caribbean, Chile). 2019. Perspectivas de la agricultura y del desarrollo rural en las Américas. Bioeconomía: Potenciando el desarrollo sostenible de la agricultura y de los territorios rurales en América Latina y el Caribe. San José, Costa Rica, IICA.
8. Ireta-Paredes, A. R., J. R. Altamirano-Cárdenas, A. V. Ayala-Garay, e I. Covarrubias-Gutiérrez. (2015). Análisis macroeconómico y microeconómico de la competitividad del arroz en México. Agricultura, Sociedad y Desarrollo. 12(4): 499-514.
9. Ireta-Paredes, A. R., L. E. Garza-Bueno, J. S. Mora-Flores, y B. V. Peña-Olvera. (2011). Análisis de la competitividad de la cadena del arroz (Oriza sativa) con enfoque CADIAC, en el sur de Morelos, México. Agrociencia. 45(2): 259-265.
10. Kapur T., Kandpal T. C., and Garg H. P. (1996) Electricity generation from rice husk in Indian rice mills: potential and financial viability. *Biomass and Bioenergy*, vol. 10, no. 5-6, pp. 393–403.
11. Le T.M., Tran U.P.N., Duong Y.H.P., Nguyen K.T., Tran V.T., Le P.K. (2022) Development of a paddy-based biorefinery approach toward improvement of biomass utilization for more bioproducts, Chemosphere 289, 133249, https://doi.org/10.1016/j.chemosphere.2021.133249.
12. Mishra P., Chakraverty A., and Banerjee H. D., (1986) Studies on physical and thermal properties of rice husk related to its industrial application *Journal of Materials Science*, vol. 21, no. 6, pp. 2129–2132.
13. Renard MC and DR Domínguez-Arista. (2019) The geographical indication of mezcal in Mexico: A tool of exclusion for small producers Geographical Indication and Global Agri-Food; Development and Democratization: 191-255.
14. Reza A. Azman H., Khaliq M. and Zainoha Z. (2015) Rice Husk Filled Polymer Composites, International Journal of Polymer Science Volume 2015, Article ID 501471, 32 pages http://dx.doi.org/10.1155/2015/501471
15. Sookkumnerd C., Ito N., and Kito K., (2005) Financial viabilities of husk-fueled steam engines as an energy-saving technology in Thai rice mills. Applied Energy, vol. 82, no. 1, pp. 64–80.
16. Stegmann P. Londo M. Junginger M.M. (2020) The circular bioeconomy: Its elements and role in European bioeconomy clusters, Resources, Conservation & Recycling: X, Volume 6,100029, https://doi.org/10.1016/j.rcrx.2019.100029.
17. Tolentino J. M. (2013) The rice production of the state of Morelos under the approach SIAL, Estudios Sociales (12) 44:39-61.
18. Torres G. (2012) "Sistemas agroalimentarios localizados. Innovación y debates des- de América Latina" en F. Boucher, A. Espinoza y M. Pensado (coords.), *Sistemas agroalimentarios localizados en América Latina.* Miguel Ángel Porrúa/Red Cien- tífica en Sistemas Agroalimentarios Localizados, pp. 35-58.
19. Torres G. and Muchnik J. (2013) "Globalization/fragmentation process: Governance and public policies for localized agri-food systems" en F. Arfani, M. Mancini y M. Donati, *Local agri-food systems in a global world: Market, social and environmental challenges.* E. U. Cambridge Scholars Publishing, New Castle upon Tyne, pp. 97-116.
20. WIPO (2022). What is a geographical indication? https://www.wipo.int/geo_indications/en/

Structural analysis of chitosan structures in interaction with Ag_2O nanoparticles by molecular dynamic simulation

Mario Pérez-Álvarez[1], Héctor Domínguez[2], Luis Vicente[3], Francisco Javier Sánchez-Ruíz[4], Javier Illescas[1], Sonia Martínez-Gallegos[1]

[1]Tecnológico Nacional de México / Instituto Tecnológico de Toluca, Av. Tecnológico S/N, Col. Agrícola Bellavista, CP 52149, Metepec, México.
[2]Facultad de Química, Universidad Nacional Autónoma de México, Circuito Exterior, Ciudad Universitaria, CP 04510, Ciudad de México, México
[3]Instituto de Investigaciones en Materiales, Universidad Nacional Autónoma de México, Circuito Exterior, Ciudad Universitaria, CP 04510, Ciudad de México, México
[4]UPAEP Universidad Popular Autónoma del Estado de Puebla, 21 Sur No. 1103, Barrio de Santiago, CP 72410, Puebla, México.

Abstract

Using molecular dynamic simulation with the COMPASS force field the structure of chitosan models is studied in combination with silver oxide nanoparticle models. The nanoparticle models of Ag_2O were obtained from geometric bases from their crystallographic structure and the simulated annealing method determined the most stable structures for the nanoparticles. On the other hand, the most stable models of chitosan oligomers were calculated from their chemical structure and the simulated annealing method was also compared the simulated Raman spectrum of the models with the one obtained experimentally. From the structural analysis of the models, their stability interaction between the chitosan systems and the nanoparticles is analyzed, allowing the obtaining of models of a material composed of chitosan-and nanoparticles of silver oxide with physical bonds type Van der Wals between the two systems. These models can be used to do computational experiments and define structural, physical, and chemical properties of a composite material.

Introduction

Chitosan polymer nanocomposites dopped with metal nanoparticles have been attracting much attention to explore their applications in the fields of medicine, food industry, textile industry and environmental applications. Chitosan is composed of molecular units of β-(1→ 4) D-glucosamine and N-acetyl-D-glucosamine [1].

On the other hand, silver dioxide nanoparticles (Ag_2ONPs) can be phytosynthesized using plants, algae, such as *Eichhornia crassipes*, whose antimicrobial properties give it useful characteristics similar to chitosan [2]. Since the chitosan polymer and phytosynthesized Ag_2ONPs share properties such as antimicrobial and biocompatibility it is important to study the compounds that can be derived from the combination of these materials.

Molecular dynamic simulation allows to identify and understand physical and chemical properties, such as the reactivity of the materials formed by chitosan and nanoparticles, as

well as their data of flexibility, stability and other properties that will allow to better understand the behavior and applications of the new composite material.

Modeling Ag_2ONPs

Models of silver oxide nanoparticles (Ag_2ONPs) were developed starting from their arrangement and crystalline locating the atomic positions in space taking the positions of the crystal growing the models of Ag_2ONPs so that they adopt the cubic shape of the crystal and then trimming the positions of the vertices of the formed cube to make the models spherical. With this method models of Ag_2ONPs were obtained (Figure 1a). Moreover, a geometric optimization was applied to these models using the "Smart Minimizer" method in the Forcite module of the Materials Studio® (MS®), and the force field "COMPASS". Subsequently, a molecular dynamic simulation was performed in the assembly (NVT) in MS® of models for particle sizes from radius 11 to 25 Å at room temperature (298 K), with a pitch size of 2 fs, and a total simulation time of 1000 ps to corroborate their stability. In the case of the relationship between the developed models of Ag_2ONPs with respect to those reported in the literature, a simulation of an image from the transmission electron microscopy (TEM) of these models was performed with the SimulaTEM software [3]. From the crystalline models and the structural results obtained from the molecular dynamics simulation, X-ray diffractograms were obtained for each of the models on the Reflex module, that are also contained in the MS®. The employed parameters to obtain the different diffractograms were those of an X-ray equipment of Brag-Bretane diffraction geometry; the origin of the radiation is Cu with a wavelength = 1.540562 Å (Figure 1b). The XRD spectra obtained was compared against the standard spectra of Ag_2O (JCPDS 12-0793) at 2θ values of 26.60, 32.73, 37.98, 54.79, 65.34 and 68.59 Bragg reflection peaks were observed, which are indexed to (110), (111), (200), (220), (311), and (222) planes of Ag_2ONPs respectively showed in (Figure 1b).

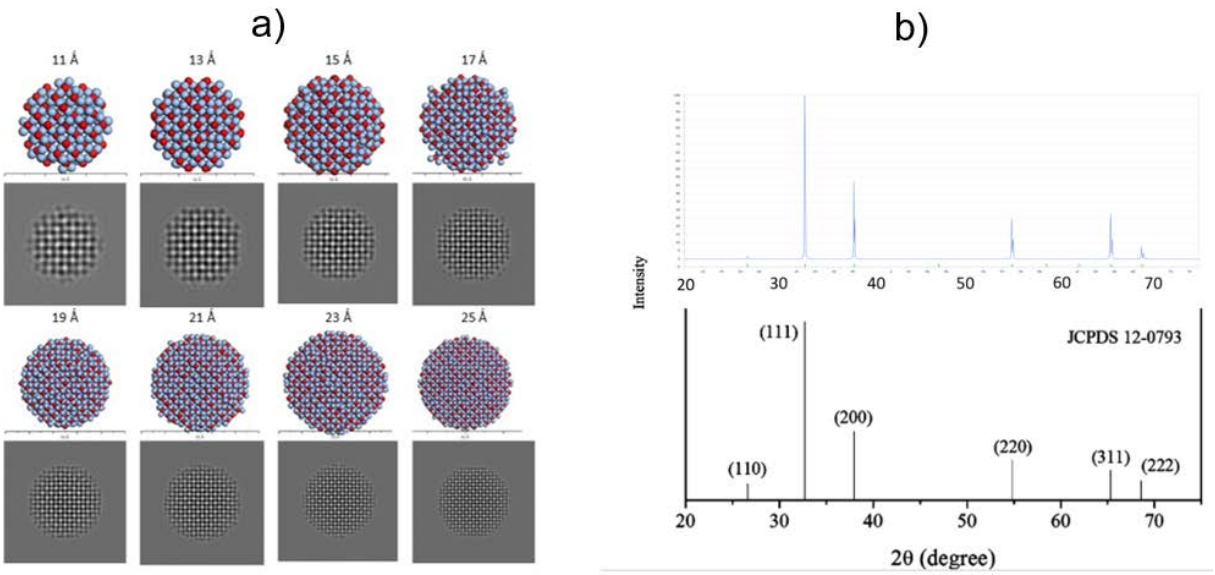

Figure 1. a) Models of Ag_2ONPs and its HRTEM images b) XRD spectra comparison with JCPDS

Modeling chitosan oligomers

A basic molecule construction tool of the MS® software was employed; with this tool some models of chitosan oligomers were drawn from the chemical structure given in the literature [4]. These models were brought to states of minimum potential energy using the computational tools of classical mechanics and quantum mechanics contained in the Materials Studio® within the Forcite module. A geometrical optimization was made with the Dmol^3 module contained in the MS®. Figure 2 shows the Raman spectra of the simulated chitosan oligomers (a) in comparison with the spectrum obtained experimentally using commercial chitosan highly deacetylated obtained from Sigma-Aldrich. The prominent Raman peaks can be assigned as the following; the C-O stretching region (1200-1300 cm^{-1}), the C-H bending region (2700-3050 cm^{-1}), N-H (3200 cm^{-1}) and O-H (3361 cm^{-1}).

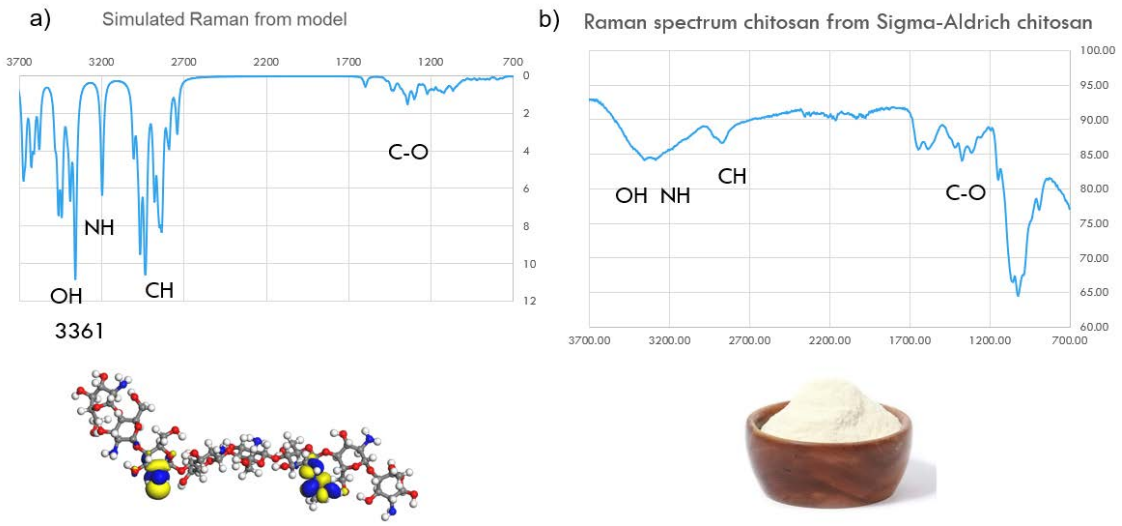

Figure 2. a) Simulated Raman spectra of chitosan, b) Experimental Raman spectra of chitosan

Simulation of Chitosan-Ag_2ONPs nanocomposite

The simulation cell was created with periodic boundary conditions using amorphous cell module in MS® with the structures at minimum energies to study various features of chitosan polymer nanocomposites systems composed. The equilibrations and relaxations of the cells have been accomplished, like temperature as well as COMPASS potential and kinetic energies are acquired by means of the molecular dynamic runs. Figure 3 reveals the chemical structures of chitosan chain, and one Ag_2ONP presents the relaxed configurations of the polymeric composites obtained in a canonical assembly (NVT) with a temperature of 298 K, a step size of 2.0 fs and a total simulation time of 1000 ps and its HRTEM simulated image and its diffraction pattern.

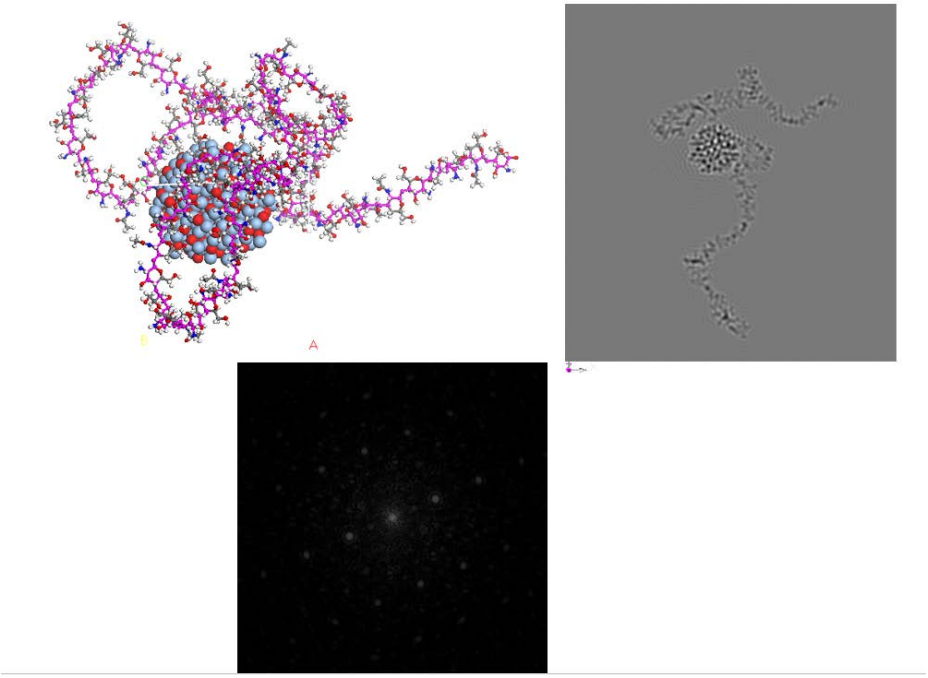

Figure 3. Chitosan-Ag_2ONP nanocomposite

Conclusions

Models of Ag_2O nanoparticle models showed good match compared to the standard spectra of Ag_2O. Also, models of crystallin chitosan polymers were designed from models of deacetylated chitosan oligomers and geometric optimization was performed, resulting in a good comparison of Raman spectra simulated vs experimental. The adsorption calculations of chitosan and Ag_2ONPs in a simulation cell showed physical interaction between the two systems resulting in a nanocomposite of these materials. The TEM simulation shows that the general appearance of the Ag_2O nanoparticles is very similar to that of the experimental samples, as well as the detection of the characteristic metallic lines for these nanoparticles.

References

[1] Giraldo, J.D., Rivas, B.L. (2020). Polym. Bull. 78, 1465–1488. https://doi.org/10.1007/s00289-020-03172-w

[2] Silva A, Martínez-Gallegos S, Rosano-Ortega G, PSchabes-Retchkiman P, Vega-Lebrún C, Albiter V., (2017),. J Nanostruct, 2017; 7(1):1-12. doi:

[3] Gómez-Rodríguez A, Beltrán-del-Río LM., Herrera-Becerra R, (2010). ISSN: 0304-3991, Ultramicroscopy, 110(2), pp. 95-104, https://doi.org/10.1016/j.ultramic.2009.09.010

https://doi.org/10.22052/jns.2017.01.001.

[4] Cunha R A, Soares T A, Rusu V H, Pontes F J S, Franca E F, Lins R D. (2012) The Complex World of Polysaccharides, Intech, http://dx.doi.org/10.5772/51803.

Preparation and characterization of luminescent grafted polyethylene films bearing natural emitters, using gamma radiation.

Ernesto Rivera[1*] and Guillermina Burillo[2]

[1]Instituto de Investigaciones en Materiales, Universidad Nacional Autónoma de México, Circuito Exterior, Ciudad Universitaria, C.P. 04510, Ciudad de México.
[2]Instituto de Ciencias Nucleares, Universidad Nacional Autónoma de México, Circuito Exterior, Ciudad Universitaria, C.P. 04510, Ciudad de México.
Email: riverage@unam.mx

Introduction

Luminescent polymers are widely used for the elaboration of many optical devices such as organic light emitting diodes (OLED's) or non-linear optical materials [1-2]. There is wide variety of luminescent fluorophores, which can be classified in function of the colour of the emitted light. Although most of the fluorophores are obtained synthetically and soluble in organic solvents, some chromophores can be extracted from natural products, and surprisingly some of them are soluble in water which make them attractive for biological applicactions. For instance, it was observed that an infusion of Palo Azul, a mexican plant employed for the treatment of kidney diseases, emits blue fluorescence when exposed to natural light. The scientific name of this plant is *Eysenhardtia Polistachya* and grows in Mexico and in the southwest of the US. Several glucosyl-hydroxichalcones have been extracted and identified from this plant [3-6]. In particular, the structure and photophysical properties of matlaline, a highly blue fluorescent dye, were investigated and reported by Acuña et al [3].

In the last years, our research group has synthesized various series of luminescent plastics based on grafted polyethylene containing photoactive groups, such as azo-dyes [12-13], pyrene derivatives [7-8], porphyrins [9], coumarins [10-11], and fluorescein [12] among others. The grafting process has been carried out using gamma radiation, which is a very effective technique. Despite the good results obtained with synthesized organic fluorophores, we decided to incorporate new fluorescent compounds such as matlaline, which is a water soluble blue emitter. This dye absorbs at 429 nm and has extinction coefficient of 33800 $M^{-1}cm^{-1}$ at pH = 9. Moreover, it reaches an emission efficiency of 100% [3], so that it can be used for the development of luminescent plastics. Besides, provided its excellent water solubility, this dye can be used as fluorescent label in DNA and other biomolecules. Herein, we report the preparation of new grafted polyethylenes containing two different emitters, one blue (matlaline) and other green (matlanine derivative), both extracted from Palo azul (Figure 1).

Figure 1. Palo azul tree (left); palo azul (middle); fluorescent solution of palo azul (right).

Materials and methods

The fluorescent dyes were extracted from Palo Azul by soaking the plant in a mixture water/EtOH (50/50 vol%) and the solvent was evaporated until dryness; then, they were separated by column chromatography in silica gel using pure ethanol as eluent. The first fractions contained the green emitting dye, whereas the blue emitting one (matlanine) was present in the last fractions. The preparation of the luminescent grafted polymers is shown in Figure 2. Firstly, the PE films were washed with methanol and dried under vacuum until constant weight. After that, they were placed in glass ampoules containing an acryloyl chloride (AC) solution in toluene (50/50 vol%); then, they were purged under vacuum, sealed and irradiated with a 60Co γ-source (Gamma beam 651 PT, Nordion International Inc.) with doses from 8 to 16 kGy at a dose rate of 9.5 kGy/h. After irradiation, the precursor grafted polymers (PE-g-AC) were washed with CH_2Cl_2 for 24 h to eliminate the residual monomer and poly(acryloyl chloride) formed as by-product. Afterwards, PE-g-AC films were placed in solutions of the natural fluorophore (blue emitter (B) or green emitter (G)) in DMSO or DMF (10mg in 50 mL) with triethylamine. The mixtures were stirred for 24 hours to afford esterification and provide the luminescent polymers PE-g-AC-B and PE-g-AC-G, which contain the blue and the green fluorophore, respectively. At last, the samples were washed with MeOH to remove the unreacted fluorophore and to convert the remaining acid chloride groups into methyl esters. The resulting films were dried under vacuum until constant weight. A PE film grafted with acryloyl and esterified only with methanol (PE-g-AC-OMe) was employed as reference to calculate the amount of grafted AC. PE-g-AC-B and PE-g-AC-G polymers were characterized by FTIR spectroscopy on a Nicolet model 510P spectrometer. Their thermal stability was determinided by thermogravimetric analysis (TGA) using a TA Instrument, model SDTQ 600 from 0 to 600 °C. Melting points (Tm) of the grafted polymers were determined by differential scanning calorimetry (DSC). A heating rate of 10 ºC/min was employed for the TGA and DSC analyses. UV-vis spectra of the grafted polymers were recorded on a CARY 100 Bio UV-Vis spectrophotometer and steady-state fluorescence measurements were recorded on a Fluorolog-3 FT311 Fluorimeter using a front-face geometry [13].

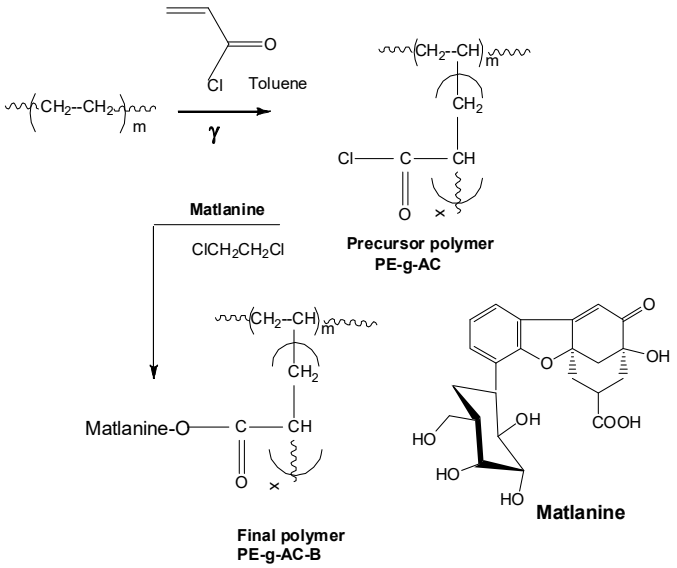

Figure 2. Synthesis of the grafted polymers containing matlanine (PE-g-AC-B).

Results and Discussion

The preparation of the grafted polymers containing natural fluorophores, PE-g-AC-B and PE-g-AC-G, is shown in Figure 2 [14]. Firstly, the precursor polymers PE-g-AC were synthesized, employing doses from 8 to 16 kGy. Then, the films were esterified in the presence of the fluorophores, G and B, using triethylamine as base to give the luminescent grafted polymers. The percentage of grafting ranged from 30–200% w/w and the amount of incorporated fluorophore varied between 5–10 w/w %. These grafted polymers showed to be resilient under ambient conditions and are not susceptible towards oxidation.

The incorporation of the fluorophores on the surface of PE film was confirmed by FTIR spectroscopy. FTIR spectra of the grafed polymers exhibited the bands of PE at 2846 and 2913 cm^{-1}, due to the –CH2– groups, followed by additional bands at 1720, 1610, 1470, 1261, and 1162 cm^{-1}, due to the C=C and C–O bonds. At last, we observed a band at 808 cm^{-1} due to the =C–H out-of-plane. Regarding the thermal properties of the modified polymers it was found that the grafting process and the incorporation of the fluorophores did not alter the crystalline microdomains of the PE matrix, since the melting points of the grafted films were almost identical to that of PE used as starting material (111 ºC). Unlikely, the thermal stability of the grafted films decreased as the amount of AC and fluorophore incorporated into the grafted PE films increased (Figure 3).

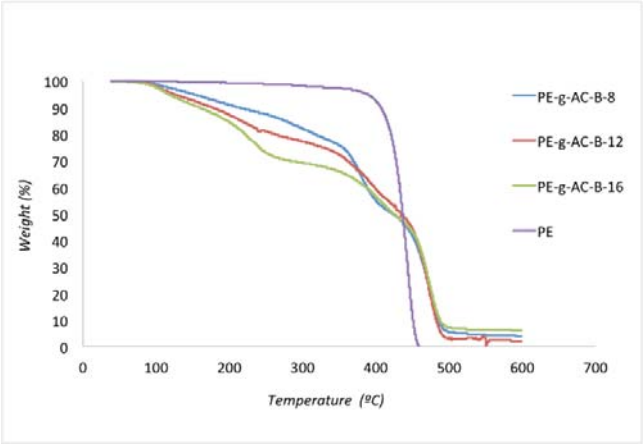

Figure 3. TGA curves of the grafted films bearing the blue emitter (PE-g-AC-B).

The optical properties of the luminescent grafted films were determined by absorption and fluorescence spectroscopies. Grafted polymer PE-g-AC-B exhibited an absorption tail at 350 nm, while PE-g-AC-G showed an absorption band at 300 nm. In both cases, a remarkable red-shift can be observed in the grafted films having the highest concentration of fluorophore. This red-shift arised from intra- and intermolecular interactions between neighbor fluorophore moieties in the grafted polymers. The emission spectra of the blue emitting films (PE-g-AC-B) (Figure 4) showed a fluorescence band at 445–460 nm, whereas the green emitting films (PE-g-AC-G) displayed two bands at 440 and 540 nm. The innovation of this contribuition is that for the first time these natural fluorophores have been incorporated into a polymer via grafting to obtain luminescent plastics. These grafted polymer films are potential prospects to be used as UV filters, blue and green emitting materials.

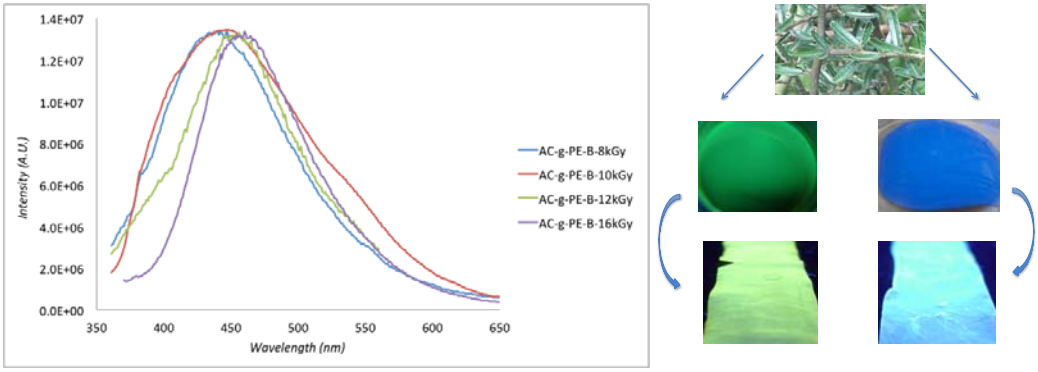

Figure 4. Normalized emission spectra of grafted polymers PE-g-AC-B (left); image of the the fluorophores and the luminescent grafted polymer films (right).

Conclusions

Two natural water soluble fluorophores were successfully extracted from the medicinal plant palo azul and further incorporated into polyethylene films by grafting, using gamma radiation. Blue and green emitting plastic films were obtained, which can be useful for the elaboration of UV filters.

References

[1] S.Günes, H. Neugebauer, N.S. Sariciftci. Chem. Rev. 107, 1324-1338 (2007).
[2] C. Li, M. Liu, N.G. Pschirer, M. Baumgarten, K. Müllen. Chem. Rev. 110, 6817-6855 (2010).
[3] A.U. Acuña, F. Amat-Guerri, P. Morcillo, M. Liras, B. Rodríguez. Organic Letters 11, 3020-3023 (2009).
[4] A.U. Acuña, F. Amat-Guerri. Springer Ser. Fluores. 4, 3-20 (2008).
[5] E. Beltrami, M. De Bernardi, G. Fronzza, G. Mellerio, G.Vidari, P.Vita-Finzi. Phytochemistry 21(12), 2931-2933 (1980).
[6] L. Alvarez, G. Delgado. Phytochemistry 681-687 (1999).
[7] A. Gelover-Santiago, M.A. Fawler, J. Yip, J. Duhamel, G. Burillo, E. Rivera. J. Phys. Chem. B 116 (21), 6203-6214 (2012).
[8] I. Valdez, S. M. Rojas-Montoya, M. Vonlanthen, E. Rodriguez-Alba, G. Burillo, E. Rivera. Rad. Phys. Chem. 153, 226-233 (2018).
[9] S.M. Rojas, M. Vonlanthen, A. Ruiu, E. Rodriguez-Alba, G. Burillo, E. Rivera. Macrom. Chem. Phys. 1800041 (2018).
[10] S.M. Rojas-Montoya, J.M. Huerta-Roldán, M. Vonlanthen E. Aguilar-Ortiz, G. Burillo, E.G. Morales-Espinoza, E. Rivera. Rad. Phys. Chem. 163, 52-57 (2019).
[11] M. Vonlanthen, S.M. Rojas-Montoya, F. Cuétara-Guadarrama, R.D. Martínez-Serrano, G. Burillo, E. Rivera. Macrom. Chem. Phys. 221(21), 2000242 (2020).
[12] S.M. Rojas-Montoya, M. Vonlanthen, F. Cuétara-Guadarrama, K. Sorroza-Martínez, G. Burillo, E. Rivera. Rad. Phys. Chem. 194, 110018 (2022).
[13] J.R. Lakowicz, Principles of Fluorescence Spectroscopy; Plenum Press: New York, 1983.
[14] R.Martinez-Serrano, A.S. Estrada-Montaño, E. Rivera, J. Illescas, G. Burillo. MRS Advances, 7(34), 1144-1149 (2022).

(empty line 12 pt)

Acknowledgements

We thank Miguel Canseco, Gerardo Cedillo and Eriseth Morales for technical assistance. We are also grateful to PAPIIT-DGAPA (Project IN103322) for financial support.

Polymat Contributions

Study of blackberry varieties *(Rubus sp.)* for their proposal in obtaining food additives

Aimme del Carmen Romero Domínguez[1], Juan Alfredo Salazar-Montoya[1], Emmanuel Flores Girón[2], Emma Gloria Ramos-Ramírez[1]*

[1]Biotechnology and Bioengineering Department, CINVESTAV-IPN, Av. Instituto Politécnico Nacional 2508, Col. San Pedro Zacatenco, México City. 07360.
[2]Agroindustrial Engineering Department, UACH, Texcoco, Edo. México.
**Email: eramos@cinvestav.mx.*

Introduction

Fruits and vegetables are considered an important part of the contemporary world diet and the main producers of functional compounds, with potential use as food additives. The name of functional foods is given to foods with beneficial properties in addition to nutritional ones; this term was first proposed in Japan, in the 1980s, to refer to FOSHU or "Foods for Specified Health Use" [1]. Among these compounds we find functional polysaccharides such as pectins and antioxidant polyphenols such as carotenoids and anthocyanins that can be used as food additives of interest to the food industry. In this sense, the fruits of blackberries (*Rubus sp*.) belonging to the group of red fruits due to their high content of flavonoids, whose antioxidant potential has been demonstrated [2] are an interesting option. Therefore, this research focused on obtaining the pectic fraction of fresh, domesticated (trademark) and wild (free growing) blackberry fruits, as well as the presence of antioxidant compounds. After conditioning the fruits, the juice and pulp fractions were separated to obtain sugars, polyphenols [3] and pectic substances at different pHs.

Materials and methods

Determination of sugars in pectin

Wild and domesticated blackberry pectins were hydrolyzed in a 6N HCl solution for 24h at 100°C, after which time they were evaporated to dryness, diluted with 1 mL of water and filtered with 0.45 µm nylon acrodiscs, and injected into the Liquid Chromatography equipment (LDC Analytical), with a refractive index detector (IR, Varian) under the following conditions Column: Rezex RMH Monosaccharide; Column temperature: 65°C; Detector Temperature: 45°C; Flow: 0.5 mL/min; Injection volume: 50 µL.

Phenolic Compounds (FC) and Antioxidant Capacity (AC)

The pectin samples of both blackberry varieties were hydrated for 12 h under agitation at 25ºC in a concentration of 2.5 mg/ml, after which time they were placed in a water bath for 2 h at 40ºC; Subsequently, they were centrifuged at 9000 rpm for 15 minutes, the supernatant was filtered with 0.45 µm nylon acrodiscs and they were kept protected from light until analysis [4]. The total phenolic compounds were determined by the Folin-Ciocalteu spectrophotometric method [5], the antioxidant capacity by ABTS and DPPH [6].

Determination of Galacturonic Acid (GA) in pectin

The presence of galacturonic acid in the pectin samples was determined by two methods, Blumenkrantz and Asboe-Hansen (1973) and Scott (1979), both techniques are based on the reaction of m-hydroxydiphenyl and 3,5-dimethylphenol respectively, from of the hot action of

sulfuric acid on galacturonic acid, with a colorimetric reagent to obtain a colored product that has an absorbance at a given maximum wavelength.

Results and Discussion

Sugars in pectin

Structurally, pectin is made up of long-chain polysaccharides composed of D-galacturonic acid units, linked together by α-1-4 bonds, chains that form polygalacturonic acid or pectic acid. In parallel, there are certain sugars that accompany pectin, such as arabinose, galactose and xylose, the use of HCl and ethanol precipitation hydrolyzes the previous sugars.

Despite carrying out an extraction process by means of acid hydrolysis, in Table 1 for the wild variety, it can be observed that the sugar concentration is determined by the extraction pH in the pectin, where the percentage of glucose is greater than pH = 2. However, Table 2 shows that in the domesticated variety the presence of this sugar is low. In both varieties the presence of arabinose was higher at pH = 2.5 and 3.5, respectively.

Table 1. Concentration of sugars present in Wild Blackberry pectin (Values expressed as a percentage).

	WILD BLACKBERRY		
	pH = 2.0	pH = 2.5	pH = 3.5
MALTOSE	2.04±0.05	2.70±0.07	2.82±0.13
GLUCOSE	13.78±0.17	7.28±0.03	9.91±0.16
GALACTOSE	3.50±0.65	3.79±0.01	2.74±0.19
RHAMNOSE	1.53±0.64	1.64±0.05	0.65±0.03
ARABINOSE	6.67±0.17	8.72±0.13	5.38±0.03

According to what has been reported in the bibliography, the proportion of neutral sugars in increasing order such as arabinose, galactose, glucose, rhamnose, fucose, xylose and mannose are present in pectin [7]. The presence of pectin is also indicated. different neutral sugars according to the proportion they occupy in the pectin structure. Therefore, in our results it was found that arabinose is the least present sugar in the wild variety, compared to the domesticated variety, and glucose is the most abundant sugar, with rhamnose being found in intermediate concentrations. Therefore, pectins extracted at lower pH values have a lower neutral sugar content than pectins extracted at higher pH values, which could be explained by the fact that at low pH values (<2), neutral sugar bonds are very sensitive to acid hydrolysis [8].

Table 2. Sugars Concentration present in Domesticated Blackberry pectin (Values expressed as percentage).

	DOMESTICATED BLACKBERRY		
	pH = 2.5	pH = 3.5	pH = 4.5
GLUCOSE	3.58±0.0	3.23±0.22	3.73±0.16
GALACTOSE	4.30±0.06	6.42±0.09	5.71±0.32
RHAMNOSE	1.57±0.09	1.68±0.35	1.31±0.10
ARABINOSE	8.49±0.22	10.01±0.35	8.15±0.37

Phenolic Compounds (PC) and Antioxidant Capacity (AC)

In Figure 1, a low concentration of phenolic compounds can be observed in both varieties; however, as the pH increases, so does the concentration of phenolic compounds.

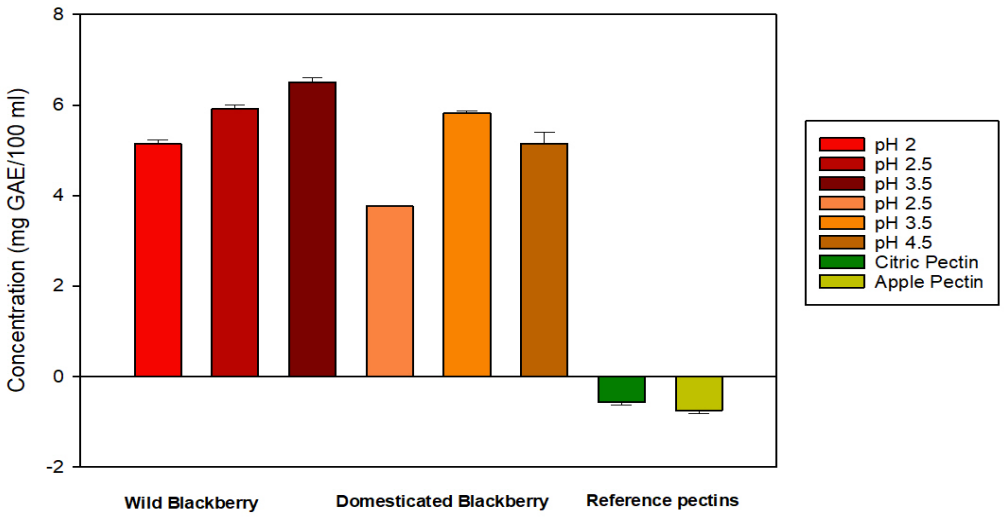

Figure 1. Phenolic Compounds present in Blackberry pectin and in reference pectins.

The ability of pectin to oxidize the DPPH radical is better compared to ABTS. Figure 2 shows that the change in pH significantly affected the inhibition percentage of each radical, observing that at pH 3.5 better results are obtained in both PC and AC for the wild variety and at pH 2.5 higher concentration of PC in the domesticated variety.

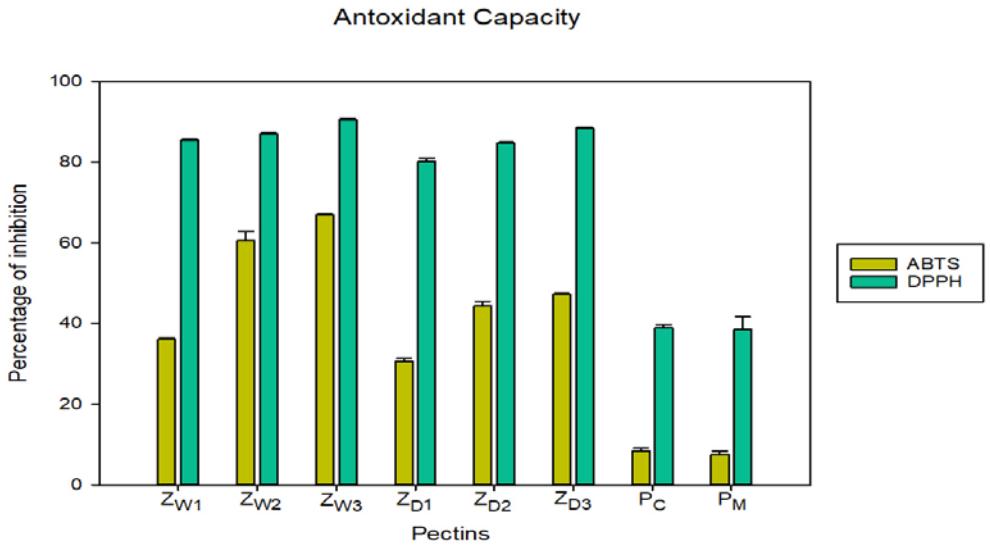

Figure 2. Percentage of inhibition of the radical ABTS and DPPH (ZS1: Wild blackberry pH 2, ZS2: pH 2.5, ZS3: pH3.5; ZD1: Domesticated blackberry ZD1: pH 2.5, ZD2: pH 3.5, ZD3: pH4.5; PC: Citrus pectin; PM: Apple pectin)

Determination of Galacturonic Acid (GA) in pectin

Within a pectin molecule, galacturonic acid is the main component, which is why its analysis is of the utmost importance since it is related to its quality, that is, the quantification allows estimating the purity of the pectin. extracted [9].

The percentage of GA in blackberry pectin in the wild variety increases according to the increase in pH in both techniques, however, Figure 3 shows that the pH with the best presence of GA, in both varieties, was pH=3.5 (ZS3 and ZD2). Even when the percentages obtained from GA are less than 65%, the functional properties that each variety contains could be helpful to complement its possible application. The determination of galacturonic acid by two methods, in Figure 3, indicates a significant difference between the pH even in the same variety, both techniques are based on spectrophotometry; therefore, the increase in the percentage of GA may be related to the sensitivity of the technique and a possible interference from the PC and AC present in the samples, since compared to the reference pectins (PC and PM) there is no difference significant in the presence of this acid by the two methods used.

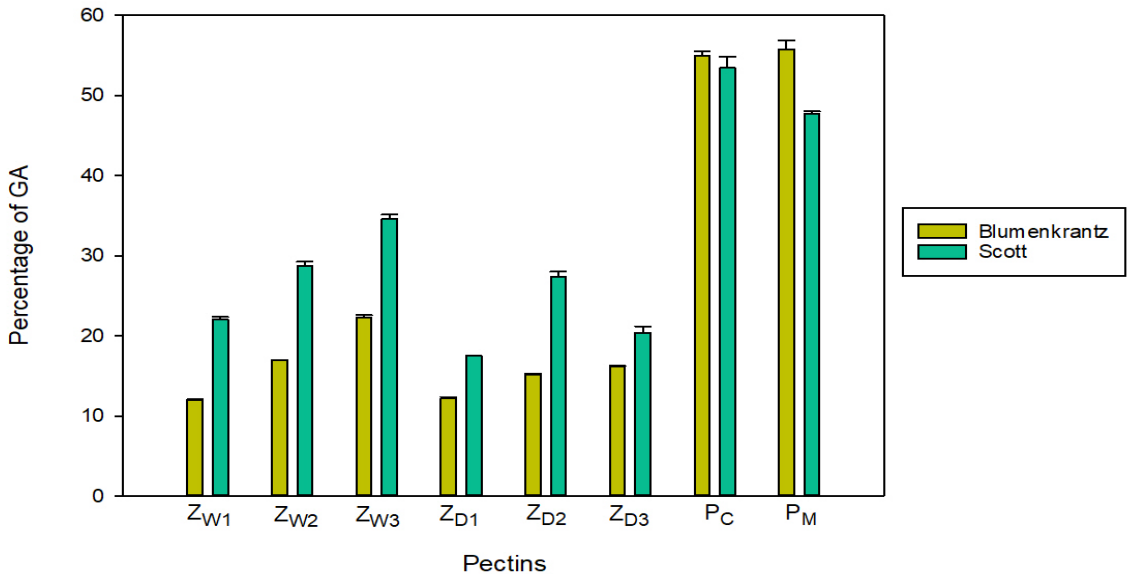

Figure 3. Galacturonic acid from Blackberry pectin and reference pectins, determined by two methods.

References

[1] Garti D N., McClements J. (2012). Encapsulation Technologies and Delivery Systems for Food Ingredients and Nutraceuticals. 1st Edition, Woodhead Publishing. eBook ISBN: 9780857095909

[2] Kaume L., Howard L.R., Devareddy L., (2012). The Blackberry Fruit: A Review on Its Composition and Chemistry, Metabolism and Bioavailability, and Health Benefits J. Agr Food Chem. 60: 5716

[3] Kuskoski, E.M, Asuero A.G., Troncoso A.M., Mancini-Filho J., Fett R, (2005). Aplicación de diversos métodos químicos para determinar actividad antioxidante en pulpa de frutos. Food Sci Tech (Campinas). 25(4): 726-732

[4] Bermúdez O A., Rodríguez G G., Rodríguez J E., González J A., Fernández B J. (2018). Molecular interactions between 3,4-dihydroxyphenylglycol and pectin and antioxidant capacity of this complex in vitro. Carbohydrate Polymers. 197: 260-268,
[5] Singlenton V L., Rossi J A. (1965). Colorimetry of total phenolics with phosphomolybdic-phosphotungstic acid reagents. Amer J Enol Viticult. 16:144–158.
[6] Thaipong K., Boonprakoba U., Crosby K., Cisneros L. and Hawkins. B. D. (2006). Comparison of ABTS, DPPH, FRAP, and ORAC assays for estimating antioxidant activity from guava fruit extracts. J. Food Compos. An. 19:669-675.
[7] Yapo, B.M (2009). Lemon juice improves the extractability and quality characteristics of pectin from yellow passion fruit by-product as compared with commercial citric acid extractant. Bioresource Technology. 100: 3147-3151.
[8] Yapo, B M., Wathelet, B., Paquot, M. (2007). Comparison of alcohol precipitation and membrane filtration effects on sugar beet pulp pectin chemical features and surface properties. Food Hydrocolloid. 21, 245–255.
[9] Perusello, C., Zhang, Z., Marzocchella, A., & Tiwari, B. (2017). Valorization of Apple Pomace by Extraction of Valuable Compounds. Comprehensive Reviews in Food Science and Food Safety, 16(5): 776–796.

Acknowledgements
The authors thank CONACyT-Mexico for the academic scholarship 777150 to the ACRD, as well as the research assistant Biol. M. Pilar Méndez Castrejón for technical support and Eng. Gustavo G. Medina Mendoza for the chromatography analysis.

Polymat Contributions

Synthesis and characterization of novel ether-bond-free aryl backbone polymers for application as anion exchange membranes.

Ernesto Sanchez[1], Lilian I, Olvera[2]

[1]Instituto de investigaciónes en Materiales, Universidad Nacional Autónoma de México, Apartado Postal 70-360, CU, Coyoacán, 04510, Ciudad de México, México
ernestosanchez190890@@gmail.com. lolvera@materiales.unam.mx

ABSTRACT

A novel linear, soluble, high-molecular-weight polymers has been obtained using a superacid-catalyzed polyhydroxyalkylation reaction of aromatic monomers and isatine. The reactions were performed at room temperature in the Brønsted superacid trifluoromethanesulfonic acid (CF_3SO_3H, TFSA) in a mixture with methylene chloride. The obtained materials were functionalized by nucleophilic substitution reactions with the aim of introducing different amino-quaternary groups (positive charges) and were also characterized by FT-IR, NMR-H^1, viscosity and TGA experiments. The two AEMs, prepared using the casting method, exhibited a conductivity of 148 and 221 mS/cm at 80 ^oC. It demonstrates its potential applicability in electrochemical devices.

Keywords: Superacid-catalyzed, polyhydroxyalkylation, Anion exchange membranes, Ether-free polymers.

1. Introduction

In recent years, energy consumption and its use by human activity has demanded the development of better electrical devices capable of storing and transforming energy.[1,2] Therefore, several technologies have been developed for this purpose, such as fuel cells, redox flow batteries, electrodialysis, hydrogen compressors and others.[2] Specifically, anion exchange membranes (AEMs) have increased their development due to their use in anionic fuel cells (AEMFCs) which, unlike protonic fuel cells, the alkaline conditions allow obtaining a faster and more efficient reduction of oxygen at the cathode, reducing the use of platinum-based catalysts and therefore decreasing the costs of this technology. [3]

2. Experimental Section.

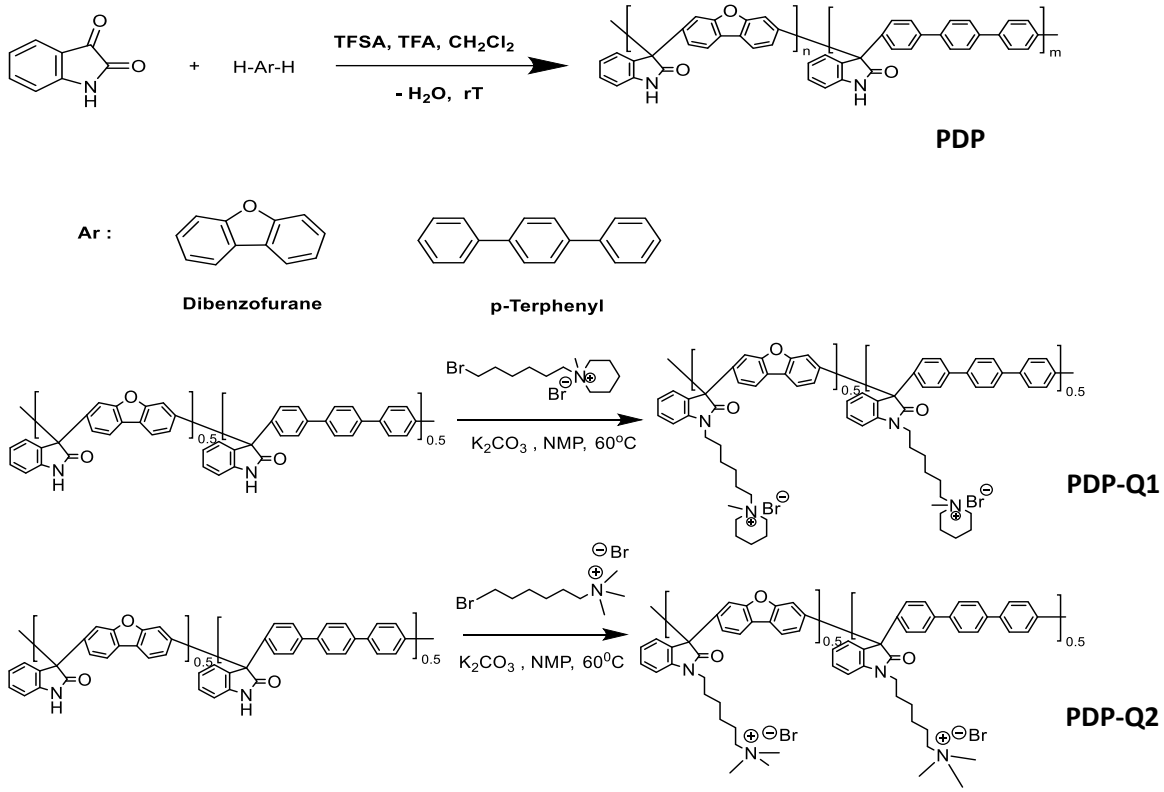

Scheme 1. Polymerization of isatin with p-terphenyl and dibenzofurane and Nucleophilic substitution.

3. Results and Discussions.

The precursor polymer was synthesized via a polyhydroxyalkylation reaction in the Brønsted superacid trifluoromethanesulfonic using as aromatic reagents dibenzofuran, p-terphenyl[2]. Subsequently, a nucleophilic substitution reaction was carried out on the amide nitrogen, to achieve the incorporation of the quaternary group. The degree of functionality in all chemical modifications was verified by FT-IR and ^{1}H NMR and analysis.

Entry	Polymer Code	Monomer Ratio	Conc. (M)	Isatine excess (%)	TFSA/Isatine (mol/mol)	Reaction time	Yield (%)	η (dL/g)
1	PDP	0.5/0.5	0.5	15	7.34	45 min	98	1.68

Table 1. Conditions of polyhydroxyalquilation reaction of isatin and dibenzofurane/p-Terfenilo.

Entry (Ratio m/n)	Polymer amount (mmol)	Modification Reagent (mmol)	K_2CO_3 (mmol)	Functionalization %	Reaction Time
1(0.5/0.5)	3.6	3.6	3.6	97.5	96 h
2(0.5/0.5)	3.6	3.6	3.6	98.3	96 h

Table 2. Conditions of nucleophilic substitution to introduce the amino-quaternary group.

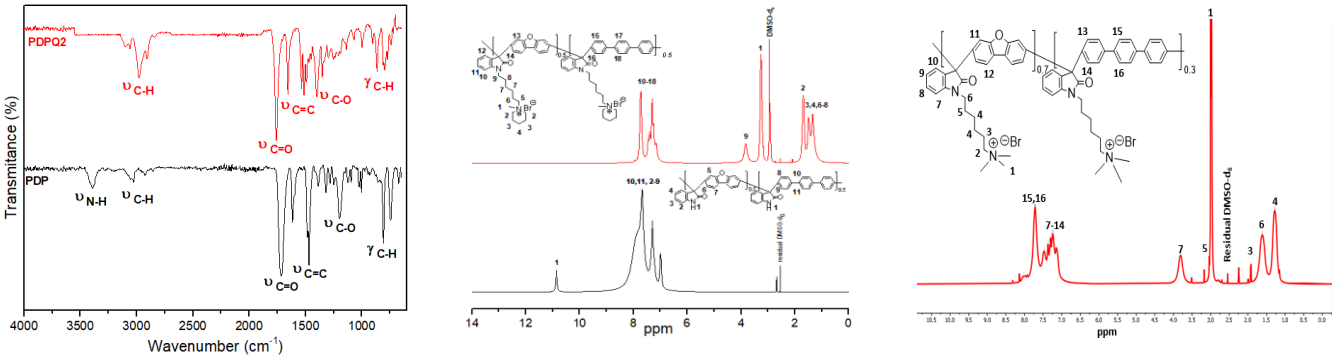

Figure 1. Left ATR-FT-IR spectra of base polymers (black line) and their modifications (red line). Right ^{1}H-NMR (400 MHz) in DMSO-d_6 spectra for copolymers and its modification.

Ref.	Properties							
	SR(%)		WU(%)		IEC (meq/g)		$^{-}$OH Conductivity (mS/cm)	
	R.t	80ºC	R.t	80ºC	Theorical	Experimental*	30ºC	80ºC
PDPQ1	4.7	6.6	14.3	42.7	2.34	2.14	74.14	148.30
PDPQ2	4.9	8.6	19.9	47.1	2.58	2.24	125.29	221.44

Table 3. Membranes properties determined at two different temperatures.

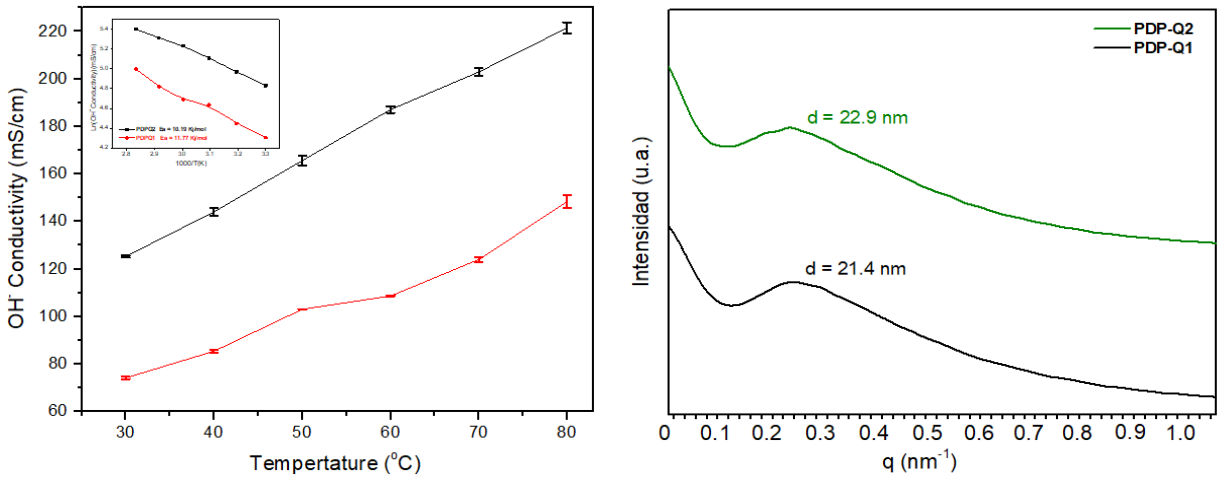

Figure 2. Left OH conductivity at different temperatures and Arrhenius plot for apparent energy activation. Right. SAXS experiment to determine de phase separation formed.

4. Conclusions.

New free-ether polymer was obtained by one-pot, superacid catalyzed non-stoichiometric step polymerization and modified by nucleophilic substitution. The polymers were characterized by spectroscopy techniques as well as their modificated solid polyelectrolytes. The AEMs also were obtained using casting method and their properties are improved at high temperature. The conductivity values were 148 and 221 mS/cm at 80 °C and SAXS experiments showed the microphase separation formed. These AEMs are a new potential device for energy exchange, storage, and generation.

References

[1] J. Ran, L. Wu, Y. He, Z. Yang, Y. Wang, C. Jiang, L. Ge, E. Bakangura, T. Xu, Ion exchange membranes: new developments and applications, J. Membr. Sci. 522(2017) 267–291.
[2] T. Luo, S. Abdu, M. Wessling, Selectivity of ion exchange membranes: a review, J. Membr. Sci. 555 (2018) 429–454.
[3] Luo, X., Kushner, D. I., & Kusoglu, A. (2023). Anion exchange membranes: The effect of reinforcement in water and electrolyte. Journal of Membrane Science, 685, 121945.

Acknowledgements: The authors acknowledge the financial support from CONACYT Mexico CB-2017-2018 A1-S-17967 and PaapiitIA102223. Msc. Gerardo Cedillo Valverde by 1 H-NMR spectra. Tec. Academic Eriseth Reyes Morales by TGA curves

POLYMAT CONTRIBUTIONS, Año 6, No. 6, enero-diciembre 2023, es una publicación anual editada por la Universidad Nacional Autónoma de México, Ciudad Universitaria, Delegación Coyoacán, C.P.04510, México, D.F., a través del Instituto de Investigaciones en Materiales, Avenida Universidad 3000, Col. Copilco, Del. Coyoacán, C.P. 04510, Ciudad de México, Tel. (55)56224500 y (55)56224581, www.iim.unam.mx/polymatcontributions, polymat@unam.mx. Editor Responsable: Dr. Ernesto Rivera García, Reserva de Derechos al uso Exclusivo No. 04-2015-110313532900-203, otorgado por el Instituto Nacional del Derecho de Autor, ISSN 2448-590X.

Responsable de la última actualización de este número, Instituto de Investigaciones en Materiales, Dr. Ernesto Rivera García, Avenida Universidad 3000, Col. Copilco, Del. Coyoacán, C.P. 04510, Ciudad de México, fecha de la última modificación, diciembre de 2023. Las opiniones expresadas por los autores no necesariamente reflejan la postura del editor de la publicación. Se autoriza la producción total o parcial de los textos aquí publicados siempre y cuando se notifique al editor.

ISSN 2448-590X